Chemical Engineering Science 287 (2024) 119679

Contents lists available at ScienceDirect

Chemical Engineering Science

journal homepage: www.elsevier.com/locate/ces

Development of a chemistry-based isotherm model and techno-economic optimization of a moving bed process for CO_2 capture using a functionalized metal-organic framework

Ryan Hughes [a], Goutham Kotamreddy [a], Debangsu Bhattacharyya [a,*], Surya T. Parker [b,c], Matthew N. Dods [b,c], Jeffrey R. Long [b,c,d], Benjamin Omell [e], Michael Matuszewski [e]

[a] Department of Chemical and Biomedical Engineering, West Virginia University, Morgantown, WV 26506, USA
[b] Materials Sciences Division, Lawrence Berkeley National Laboratory, Berkeley, CA 94720, USA
[c] Department of Chemical and Biomolecular Engineering, University of California, Berkeley, CA 94720, USA
[d] Department of Chemistry, University of California, Berkeley, CA 94720, USA
[e] National Energy Technology Laboratory, 626 Cochrans Mill Road, Pittsburgh, PA 15236, USA

ARTICLE INFO

Keywords:
Metal–organic framework
Carbon capture
Chemistry model
Temperature swing adsorption
Techno-economic analysis

ABSTRACT

Amine-appended metal–organic frameworks of the class Mg_2(dobpdc) are promising candidates for efficient carbon capture in part due to their step-shaped CO_2 adsorption behavior. However, the existing isotherm models are lacking as they are unable to capture the complicated chemisorption mechanisms which are still not well known for these materials. Here, a chemistry-based isotherm model is developed and fit to experimental CO_2 adsorption data for dmpn-Mg_2(dobpdc). Reactions for a cooperative adsorption mechanism are proposed, and the reaction pathway is optimally selected. The chemistry-based model shows an improvement in prediction by a factor of 6 when compared to a recent isotherm model in literature. A plant-wide model is developed for a moving bed based adsorber/desorber and techno-economic optimization is performed. For likely values of price and lifespan, the moving bed process gives a significant improvement in economics when compared to a fixed bed contactor process and a traditional MEA capture system.

1. Introduction

Aqueous amine solutions are currently the only mature technology for post-combustion from fossil fuel-based power generation plants; however, the significant energy penalty associated with the regeneration of these solutions and their corrosive nature has precluded their wide-spread implementation and motivated diverse research investigating alternative sorbent materials for efficient CO_2 capture (Sumida et al., 2012). Among these materials, amine-appended frameworks of the type amine–Mg_2(dobpdc) (dobpdc^{4-} = 4,4′-dioxidobiphenyl-3,3′dicarboxylate) have emerged as leading candidates for CO_2 capture. The majority of these adsorbents capture CO_2 via a unique cooperative chemisorption mechanism involving CO_2 insertion into the metal–amine bond and the formation of chains of ammonium carbamate down the framework channels. Importantly, the step-shaped CO_2 adsorption profiles associated with this chemisorption endow these materials with much higher working capacities when compared to traditional Langmuir-type adsorbents (Kim et al., 2020; McDonald et al., 2015; Milner et al., 2017). Further, by varying the appended amine, it is possible to tailor the CO_2 adsorption step pressure (temperature) to the capture application of interest (Siegelman et al., 2017). One of these adsorbents, dmpn–Mg_2(dobpdc) (dmpn = 2,2-dimethyl-1,3-diaminopropane), exhibits stepped CO_2 uptake at 40 °C and ~15 mbar and retain a stable CO_2 capacity over the course of 1000 humid CO_2 adsorption/desorption cycles, and as such it is a promising candidate for post-combustion CO_2 capture from coal flue gas (Milner et al., 2017).

When evaluating the potential of any candidate adsorbent technology for CO_2 capture, design and optimization of potential capture processes using mathematical models is critical to enable a realistic understanding of energy penalties associated with capture and how these can be minimized. It is particularly important to accurately predict the adsorption equilibrium and how it changes with operating conditions, specifically temperature and partial pressure, over the entire expected range for adsorption and desorption. The prediction of adsorption equilibria for solid adsorbents is typically done using

* Corresponding author.
E-mail address: Debangsu.Bhattacharyya@mail.wvu.edu (D. Bhattacharyya).

https://doi.org/10.1016/j.ces.2023.119679
Received 4 October 2023; Received in revised form 7 December 2023; Accepted 22 December 2023
Available online 29 December 2023

Nomenclature

MB	Moving bed
MOF	Metal-organic framework
MEA	Monoethanolamine
TSA	Temperature swing adsorption
Am	Unreacted dmpn amine
CO_2^*	Adsorbed phase CO_2
B, C	Cooperatively adsorbed species
MINLP	Mixed integer nonlinear programming
AIC	Akaike information criterion
CTP, CL	Tube count constants
DSF	Drive safety factor (=2)
EAOC	Equivalent annual operating cost
NETL	National energy technology laboratory
a_H	Henry's parameter [Pa]
A_1	Cross-sectional area of a repeating single tube unit in the reactor [m^2]
b_H	Henry's parameter [K]
C_g	Gas phase concentration [mol/m^3]
C_{surf}	Surface concentration [mol/m^3]
C_p	Specific heat capacity [kJ/kg/K]
$Cost_{dist}$	Cost of distributors within the moving bed reactor [$MM]
D_z	Axial dispersion coefficient [m^2/s]
d_p	Particle diameter [m]
D_b	Bed diameter [m]
D_H	Discharge height [m]
E_{phys}	Langmuir isotherm parameter [kJ/mol]
$\hat{f}^v_{CO_2}, \hat{f}^s_{CO_2}$	Vapor phase fugacity and solid phase fugacity [Pa]
$f^0_{CO_2}$	Reference state CO_2 fugacity [Pa]
J_s	Axial solids flux [kg/m^2/s]
k_{H,CO_2}	Henry's parameter [Pa]
K_{eq}	Equilibrium coefficient [-]
k_0	Equilibrium coefficient parameter [-]
k_1	Equilibrium coefficient parameter [K]
K_L	Langmuir isotherm term [Pa^{-1}]
$k_{phys,0}$	Langmuir isotherm parameter [Pa^{-1}]
k_{OC}	Solid mass transfer coefficient for the chemisorbed species [s^{-1}]
k_{OP}	Solid mass transfer coefficient for the physisorbed species [s^{-1}]
k_f	Film mass transfer coefficient [m/s]
H	Enthalpy [kJ/kmol]
h	Heat transfer coefficient [kW/m^2/K]
N, M	Number of cooperatively adsorbed species reactions
n, m	Stochiometric coefficients
N_{phys}	Langmuir isotherm parameter [mol/kg]
N_{tube}	Number of embedded heat exchanger tubes
P	Pressure [bar or Pa]
Pe'	Peclet number [-]
P_t	Tube pitch [m]
P_{BE}	Power required by bucket elevators [kW]
q^*	Equilibrium loading [mol/kg]
q	Particle loading [mol/kg]
Q	Total adsorbed phase loading [mol/kg]
Q_{CEX}	Cross exchanger duty [kW]
R	Ideal gas constant [kJ/mol/K]
Re_p	Particle Reynolds number [-]
Sc_p	Particle Schmidt number [-]
T	Temperature [K]
T_0	Reference temperature, 298 K
t	Time [seconds]
U_{CEX}	Universal cross exchanger heat transfer coefficient [kW/m^2/K]
v	Superficial velocity [m/s]
$\dot{V}_{BE}$	Solids volumetric flowrate [m^3/hr]
w_{thx}	Heat exchanger tube width [m]
y	Gas phase mole fraction [-]
z	Adsorbed phase mole fraction [-]
$\hat{\phi}_{CO_2}$	Vapor-phase fugacity coefficient [-]
γ_{CO_2}	CO_2 activity coefficient [-]
τ_A, τ_B	Activity coefficient interaction parameters [-]
$\tau_{A,0}, \tau_{B,0}$	Estimated interaction parameters [-]
$\tau_{A,1}, \tau_{B,1}$	Estimated interaction parameters [K]
δ	Total number of amine sites/CO_2 molecules in a chemisorption product
ΔH_{CO_2}	Heat of adsorption [kJ/mol]
Σ	Weighting function for chemistry model parameter estimation
ε_b	Bed voidage [-]
ρ_p	Solid particle density [kg/m^3]
$\frac{\partial Q}{\partial t}$	Mass transfer rate between the gas and solid phase [mol/kg/s]
u_{mf}	Minimum fluidization velocity [m/s]
μ_g	Viscosity [Pa•s]
ΔT_{LM}	Log mean temperature driving force [K]

Common Subscripts

i	Species
chem	Chemisorption
phys	Physisorption
g	Gas phase
s	Solid phase
p	Particle
t, tube	Tube
w	Heat exchanger tube wall
ads	Adsorber
des	Desorber
HX	Heat exchanger

traditional "off the shelf" isotherm models, such as the Langmuir or Sips models (Foo and Hameed, 2010). However, many of these traditional isotherm models have been historically developed for adsorbents exhibiting physisorption, and as such, they may not adequately capture complicated isotherm behavior that may be exhibited by a functionalized sorbent. In a few cases, however, traditional isotherm models have been altered and expanded upon in an effort to accurately prediction CO_2 adsorption equilibria in amine-appended Mg_2(dobpdc) materials (Hefti et al., 2016; Hughes et al., 2021; McDonald et al., 2015, 2012; Pai et al., 2019). For example, CO_2 uptake in mmen-M_2(dobpdc) (mmen = N,N′-dimethylethylenediamine), was modeled using piecewise modified Langmuir-Freundlich equations for pre- and post-step behavior (McDonald et al., 2015, 2012), but this disjunctive approach renders it unacceptable for use in process modeling and optimization. Notably, the weighted dual-site Langmuir model used by Hefti et al. (Hefti et al., 2016) was able to accurately predict the CO_2 adsorption profiles for mmen–M_2(dobpdc) (mmen = N,N′-dimethylethylenediamine; M = Mg, Mn, Fe, Co, Zn). Recently, Pai et al. (Pai et al., 2019) separately modeled chemisorption and physisorption of CO_2 in mmen–Mg_2(dobpdc) and used both single-site and dual-site Langmuir models to fully describe the

adsorption data. We have previously proposed a modified, dual-site Sips isotherm model to accurately predict CO_2 adsorption equilibria in dmpn–Mg_2(dobpdc) (Hughes et al., 2021). Many of these isotherm models are heuristic and may give good fits to experimental data, but do not give any insight into the underlying adsorption mechanisms. Additionally, many of the isotherm models are developed for physisorption mechanisms and are incapable of capturing underlying chemisorption mechanisms which can give important insight into process performance and behavior.

Development of chemistry-based isotherm models for functionalized solid sorbents can be beneficial for improving the current understanding the reaction mechanisms, which may not be well known or well understood for novel sorbents, especially because of the difficulty of identifying species formed and measuring their evolving concentration with operating conditions at the interior of solids. A chemistry-based model also can improve the accuracy of the CO_2 adsorption capacity to experimental data as well as improve the modeling fidelity by quantifying interactions of other species present in flue gas, specifically water, and calculating a more accurate estimate of heat of adsorption. Additionally, a chemistry model may also aid in the development of new sorbent technologies. In particular, transient products that are formed during adsorption can be difficult to detect and quantify in real-time, and a chemistry model that can predict adsorption equilibrium, adsorption products, and heats of adsorption can reduce the need for complex experimental investigations and reduce the time it takes to identify new possible sorbent variants and aid in the development of new technologies.

Currently, there are few chemistry-based models for solid sorbents in the literature that include reactions between adsorbate and adsorbent (Abdollahi-Govar et al., 2015; Lee et al., 2007a; Lee et al., 2007b; Lee et al., 2008; Liu, 2015). The models follow a similar structure: formulation of reactions specific to the system of interest, kinetic equation formulation for the reactions of interest, and solutions of the model for either kinetic or equilibrium conditions. These chemistry-based models do an adequate job at predicting either the kinetic or equilibrium data for their respective sorbents, but the adsorption equilibrium behavior of amine-appended MOFs is significantly different than the sorbents for which these chemistry models were developed, specifically the sensitivity of the CO_2 loading to temperature and pressure. For the chemistry-based models referenced above, significant additions would be required for them to accurately predict the adsorption equilibrium behavior of amine-appended MOFs being considered for carbon capture.

Recently, Kundu et. al (Kundu et al., 2018) presented an adsorption equilibrium model which is a combination of quantum and statistical mechanics that is able to predict the step-shaped adsorption profiles for mmen–Mg_2(dobpdc). The model, described as a lattice model, is informed and parameterized using density-functional theory and accounts for the presence of chemisorption products that form via a cooperative adsorption mechanism. Marshall (Marshall, 2022) has taken this lattice model and made the equations suitable for use in process simulation. The author also performs parameter estimation for low CO_2 concentration ($P_{CO2} < 100$ mbar) data for mmen–Mg_2(dobpdc) and the model shows a good fit to the data. This lattice model is one of the only models currently available that attempts to model the cooperative adsorption mechanism for amine-appended Mg_2(dobpdc). However, dmpn–Mg_2(dobpdc) is known to form two different chemisorption products forming both ammonium carbamate species at very low pressures and also a major product that is a mixture of ammonium carbamate and carbamic acid species in an approximate 1:1 ratio (Forse et al., 2018). The lattice model presented by Marshall (Marshall, 2022) is derived for only a single cooperatively adsorbed species, and re-estimation of the model parameters and subsequent analysis of the results would be required to evaluate if this lattice model is applicable to dmpn-Mg_2(dobpdc). Also of note, none of the works noted above have considered heat of adsorption as a constraint while developing the chemistry models and estimating the kinetic parameters. However, as the equilibrium adsorption and heat of adsorption are thermodynamically related, heat of adsorption should be considered as a constraint while estimating the parameters of the chemistry model for thermodynamic consistency.

Contactor technology plays a key role in obtaining the maximal performance of solid sorbents (Bhattacharyya and Miller, 2017). While the contactor technology for solvent-based capture is often absorber/stripper, selection of the appropriate contactor technology for solid-

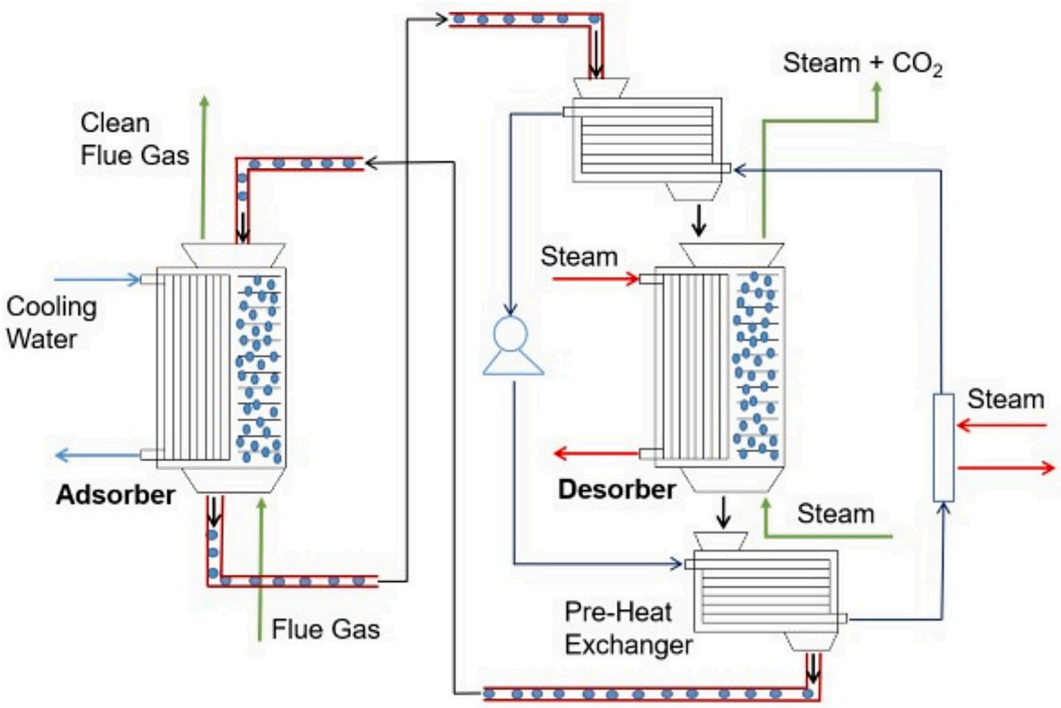

Fig. 1. Illustration of the moving bed TSA process considered in this work.

based capture is not straightforward. Optimal selection of the contactor technology among the potential technologies- such as fixed beds of various types, moving beds, and fluidized beds- not only requires consideration of material characteristics such as particle attrition resistance but also satisfactory evaluation of performance characteristics of the contactor (Bhattacharyya and Miller, 2017). Therefore, detailed modeling of the contactor technology is extremely important when designing and evaluating novel capture processes. Few models exist in literature for the contactors for the amine-appended MOF capture processes, and most of these studies consider fixed bed processes (Ga et al., 2021; Hefti et al., 2016; Joss et al., 2017; Marshall, 2022; Pai et al., 2019). Previously, the authors of this work have presented a process model of a (TSA) process for dmpn–Mg_2(dobpdc) and have shown that the technology, with efficient thermal management, can compete economically with a traditional monoethanolamine (MEA)-based post-combustion capture process (Hughes et al., 2021). Efficient heat removal/addition is challenging in fixed beds due to limiting heat transfer coefficient between the gas phase and stagnant solid phase in a fixed bed. It has also been reported in our previous work that depending on the mass and heat transfer characteristics, a considerable amount of the bed may be underutilized when the breakthrough happens in a fixed bed design (Hughes et al., 2021). Obviously, underutilization of the bed material will lead to a higher capital cost. Furthermore, recovery of the residual heat from the solids at the end of desorption and utilization of that heat for pre-heating the solids at the end of adsorption step before solids undergo desorption are crucial for reducing the energy penalty. Moving beds (MBs) can address, to a great extent, many of the drawbacks of the fixed bed processes mentioned above. Additionally, as moving beds operate under much milder flow regime compared to the fluidized beds, they have great potential for MOFs that generally cannot withstand strong attrition. Moving beds continuously operate with solid particles entering at the top of the bed while gas enters at the bottom and flows upward through the moving solid particles (see Fig. 1). This counter-current flow pattern results in large driving forces for mass and heat transfer. To the best of our knowledge, there is no paper in the open literature on the modeling of the MB-based CO_2 capture process using a diamine-appended MOF. Furthermore, the existing literature for the MB-based CO_2 capture processes has mainly evaluated energetics, recovery, and efficiency, but not the complete economic analysis considering capital and operating costs. Techno-economic process analysis is necessary for evaluating the critical tradeoff between capital and operating expenditures.

In this work, a chemistry model for the adsorption of CO_2 on dmpn–Mg_2(dobpdc) is developed for the first time. Based on what is known from experiments about the adsorption of CO_2 in this material, we modeled the chemisorption using two different reaction sets. The parameters for each reaction set are optimally estimated using least-squares fitting to available isotherm data. Additionally, the isosteric heat of adsorption is implemented as an inequality constraint in the parameter estimation problem, which, as noted above, is not typically done for chemistry-based model development. The framework for the chemistry model developed in this work is also generic and the approach can be applied to other chemisorbents by incorporating suitable reaction pathways. A detailed model for a moving bed contactor is then developed using the chemistry-based adsorption equilibrium model and a mass transfer model (Hughes et al., 2021), and is then used to simulate a moving-bed TSA capture process. Techno-economic optimization is then performed, and the results are compared to a state-of-the-art MEA process.

2. Methods and model development

2.1. Chemistry model

In this section, we present the equations for a chemistry-based model to describe the equilibrium CO_2 adsorption behavior for dmpn–Mg_2(dobpdc). The model assumes that CO_2 adsorption initially proceeds through an adsorbed phase "free" CO_2 which is in equilibrium with CO_2 in the vapor phase. This adsorbed CO_2 then reacts with the metal-bound amines to form the chemisorption products, with relative concentrations determined by the set of equilibrium relationships for each reaction that is being considered. Additionally, balance equations such as the mole fraction summation and amine site balance are used to calculate the loadings of each participating species and importantly the total loading of CO_2. A simple Langmuir model is also considered to predict the adsorption of the physisorbed CO_2 product. The isosteric heat of adsorption is calculated as a part of the model and is implemented as an inequality constraint during parameter estimation. While some chemistry models have used the heat of adsorption for qualitative evaluation and validation, to our knowledge, no reported models have used the heat of adsorption during estimation of the model parameters or in the model development stage. Optimal selection of the reaction set was carried out using an information criterion to avoid over-parameterization of the model. The framework for the chemistry model developed in this work is also generic and can be applied to any chemisorbent. Modeling and parameter estimations were performed in an equation-oriented framework and solved as a nonlinear programming problem, which allows for the adsorption reactions to be changed without the need for a complex and a time-consuming analytical solution (if one even exists). The solid–vapor equilibrium equation is independent of the sorbent chemistry and the additional equations, such as mole fraction summation and site balance, are only dependent on the stoichiometry of the adsorption reactions. Additionally, the heat of adsorption equation can be a generic equation, such as the isosteric prediction used in this work or a user defined equation in the parameter estimation framework.

2.1.1. Solid-Vapor equilibrium and activity coefficient modeling

The relationship between the gas-phase CO_2 and free CO_2 is determined by equating the fugacity of the solid phase and the vapor phase, shown in Eqs. (1) and (2).

$$\widehat{f}^{v}_{CO_2} = \widehat{f}^{s}_{CO_2} \tag{1}$$

$$y_{CO_2}\widehat{\phi}_{CO_2}P = \gamma_{CO_2} z_{CO_2^*} f^0_{CO_2} \tag{2}$$

Vapor-phase fugacity is calculated using the partial pressure of CO_2 and the vapor-phase fugacity coefficient ($\widehat{\phi}_{CO_2}$). In this work, it is assumed that the vapor phase behaves ideally ($\widehat{\phi}_{CO_2} = 1$). The solid-phase fugacity is calculated using the CO_2 activity coefficient (γ_{CO_2}), the mole fraction of free CO_2 ($z_{CO_2^*}$), and a reference state CO_2 fugacity ($f^0_{CO_2}$). The activity coefficient is modeled using a multicomponent Margules equation (O'Connell and Haile, 2005) shown in Eq. (3) and only considers binary interaction parameters for the free CO_2 and an amine which has not reacted yet, simply denoted as *Am*.

$$\ln\left(\gamma_{CO_2}\right) = z_{Am}\left[\tau_A - \tau_B\left(z_{Am} - 2z_{CO_2^*}\right)\right] - z_{CO_2^*} z_{Am}\left[\tau_A + 2\tau_B\left(z_{CO_2^*} - z_{Am}\right)\right] \tag{3}$$

In Eq. (3), τ_A and τ_B are interaction parameters of the activity coefficient model for free CO_2 and dmpn, respectively, and vary with temperature according to Eqs. (4) and (5).

$$\tau_A = \tau_{A,0} + \frac{\tau_{A,1}}{T} \tag{4}$$

$$\tau_B = \tau_{B,0} + \frac{\tau_{B,1}}{T} \tag{5}$$

The reference state fugacity is modeled using Henry's Law, as shown in Eqs. (6) and (7) (Morgan et al., 2017).

$$f^0_{CO_2} = k_{H,CO_2} \tag{6}$$

$$\ln\left(k_{H,CO_2}\right) = a_H + \frac{b_H}{T} \tag{7}$$

2.1.2. dmpn–Mg_2(dobpdc) chemistry and reaction modeling

As discussed above, dmpn–Mg_2(dobpdc) material is unique among the amine–Mg_2(dobpdc) materials studied to date in that it reacts with CO_2 to form a mixed chemisorption product consisting of chains of ammonium carbamate that interact via hydrogen bonding with carbamic acids at neighboring sites across the framework channel (Forse et al., 2018; Milner et al., 2017). Forse et al. (Forse et al., 2018) used solid-state NMR spectroscopy to study CO_2 chemisorption in dmpn–Mg_2(dobpdc) and found that while the mixed product is the dominant product at all partial pressures of CO_2, pure ammonium carbamate chains that are not interacting with carbamic acid species are also formed in small quantities at low partial pressures. Additionally, the presence of a physisorbed CO_2 species is confirmed in these NMR studies. Water is expected to alter the mechanisms of adsorption of CO_2 onto dmpn-Mg_2(dobpdc), but it has been shown experimentally using column breakthrough data to have a small effect on total CO_2 uptake (Milner et al., 2017). Incorporating water effects would require well characterized adsorption equilibrium data capturing the effect of water concentration on CO_2 loading over a range of pressure and temperature expected for post-combustion capture. However, such data are not currently available. Therefore, at this stage of development of the chemistry-based isotherm modeling, the chemistry and reaction modeling presented in this section only consider the adsorption of pure CO_2.

Given this evidence of two distinct chemisorption processes, we considered two different product formation reactions in our chemistry model. Our model was developed based on the hypothesis that the product formation in each case proceeds in multiple steps, see reactions R(1)–R(3) for formation of the first product and R4–R6 for formation of the second product below. For example, the first step in both scenarios is an initiation reaction (R1 or R4) in which some number of CO_2 molecules (n_1 or m_1) reacts with the same number of amine sites to form an initial product (B_1 or C_1, respectively). Here, only a single type of amine site is considered (Am). Then, a series of propagation reactions occur in which the product formed in the initiation reaction grows by stoichiometric coefficient (n_i or m_i). The variables N and M in R3 and R6, respectively, correspond to the total number of reactions considered. It should be noted here that since the formation reactions proposed below are equivalent, that is they do not distinguish between chemisorbed species (i.e., the mixed product or ammonium carbamate only), and therefore models with reversed values for N and M are equivalent. For example, a model with N=1 and M=0 is equivalent to a model with N=0 and M=1.

Note, all the above reactions were developed assuming a 1:1 reaction between CO_2 and the appended diamine, as has been established in previous studies (McDonald et al., 2015; Milner et al., 2017). To summarize, the model considers two main products, B and C, which are present as a varying number of chains of varying sizes (B_1, B_2, B_N, C_1, C_2, C_N, etc.). Reactions R1-R3 encompass all the chain formation reactions for product B and reactions R4-R6 encompass all the chain formation reactions of product C. The stochiometric amounts of CO_2 in these reactions (n_i and m_i) which determines the chain sizes and the number of reactions/number of chains needed to accurately predict the adsorption behavior (N and M) were determined in this work.

$$n_1 CO_2^* + n_1 Am \rightleftharpoons B_1 \tag{R1}$$
$$n_2 CO_2^* + n_2 Am + B_1 \rightleftharpoons B_2 \tag{R2}$$
$$\vdots$$
$$n_N CO_2^* + n_N Am + B_{N-1} \rightleftharpoons B_N \tag{R3}$$

$$m_1 CO_2^* + m_1 Am \rightleftharpoons C_1 \tag{R4}$$
$$m_2 CO_2^* + m_2 Am + C_1 \rightleftharpoons C_2 \tag{R5}$$
$$\vdots$$
$$m_M CO_2^* + m_M Am + C_{M-1} \rightleftharpoons C_M \tag{R6}$$

The equilibrium relationship for the reactions considered in this work and the temperature dependency of the equilibrium coefficient are shown in Eqs. (8) and (9), respectively.

$$K_{eq,j} = \prod_{i=1}^{J} z_i^{\nu_i} \tag{8}$$

$$ln\left(K_{eq,j}\right) = k_{0,j} + \frac{k_{1,j}}{T} \tag{9}$$

Here, K_{eq} is a dimensionless, mole fraction-based equilibrium coefficient developed assuming an elementary relationship in which the exponent for each species is equal to the stochiometric coefficient. The equilibrium coefficient varies with temperature according to the correlation in Eq. (9).

2.1.3. Component and site balances

The mole fraction of each species is related by the mole fraction summation as shown in Eq. (10)

$$z_{Am} + z_{CO_2^*} + \sum_{j=1}^{N} z_{B_j} + \sum_{j=1}^{M} z_{C_j} = 1 \tag{10}$$

The equilibrium loading (q_i^*) for each product and species predicted by the chemistry model can be calculated using Eq. (11).

$$q_i^* = Q \cdot z_i \tag{11}$$

Here, Q is the total loading of the system which can be determined by solving an amine site balance shown in Eq. (12). The amine site balance relates the number of amine sites contained in the chemisorption reactants and products (left-hand side of the equation) to the total number of amine sites present on the MOF (right-hand side of the equation), which is a value that has been determined experimentally to be 3.82 mol/kg (Milner et al., 2017).

$$q_{Am}^* + \sum_{j=1}^{N} \delta_{B_j} \cdot q_{B_j}^* + \sum_{j=1}^{M} \delta_{C_j} \cdot q_{C_j}^* = Q_{Am} \tag{12}$$

Here, δ is defined as the number of amine sites in the chemisorption product of interest. This value can be determined by taking the sum of the stochiometric coefficients for the formation reaction of the product of interest as well as all preceding reactions, as shown in Eqs. (13) and (14).

$$\delta_{B_j} = \sum_{i=1}^{j} n_i \tag{13}$$

$$\delta_{C_j} = \sum_{i=1}^{j} m_i \tag{14}$$

The loading of chemisorbed CO_2 can be determined in a similar manner using a CO_2 balance, shown in Eq. (15). Since the stochiometric ratio between CO_2 and amine is 1:1, the number of CO_2 molecules contained in a chemisorption product is equal to the number of amine sites and can therefore also be represented by δ.

$$q_{CO_2,chem}^* = \sum_{j=1}^{N} \delta_{B_j} \cdot q_{B_j}^* + \sum_{j=1}^{M} \delta_{C_j} \cdot q_{C_j}^* \tag{15}$$

As previously mentioned, the model also considers CO_2 physisorption represented by the Langmuir isotherm equation, shown in Eqs. (16) and (17) (Ruthven, 1984).

$$q^*_{CO_2,phys} = N_{phys}\left(\frac{K_L \cdot y_{CO_2} P}{1 + K_L \cdot y_{CO_2} P}\right) \tag{16}$$

$$K_L = k_{phys,0} \cdot \exp\left[\frac{-E_{phys}}{RT_0}\left(\frac{T_0}{T} - 1\right)\right] \tag{17}$$

Finally, the total amount of CO_2 adsorbed can be calculated by summing the loading of free CO_2, chemisorbed CO_2, and physisorbed CO_2.

$$q^*_{CO_2,tot} = q^*_{CO_2{}^*} + q^*_{CO_2,chem} + q^*_{CO_2,phys} \tag{18}$$

2.1.4. Heat of adsorption

The heat of adsorption can be estimated using the isosteric heat of adsorption equation (Lee et al., 2007a) for each loading of interest.

$$\left.\frac{\partial[\ln(P)]}{\partial T}\right|_{q^*_{CO_2}} = \frac{\Delta H_{CO_2}}{RT^2} \tag{19}$$

2.2. Reaction set selection and parameter estimation

Parameters N and M, which correspond to the number of chain formation reactions, are integer variables, which in turn make this reaction set selection and parameter estimation problem a mixed integer nonlinear programming (MINLP) problem. However, the number of equations, variables, constraints, and the overall structure of the model will change as the N and M variables change. Therefore, relaxation of these integer variables to continuous variables for obtaining bounds, as is done in many MINLP algorithms, is not acceptable. While the MINLP problem can be solved by many algorithms (including variants of Branch and Bound algorithms or *meta*-heuristic algorithms), the values of N and M are expected to be low for this problem, and therefore exhaustive enumeration was used to obtain globally optimal solution for N and M. The corresponding nonlinear programming (NLP) subproblem shown below in Eq. (20) was solved for each combination of N and M.

$$\begin{aligned} \min_{\theta} \quad & \left(q^*_{CO_2,exp} - q^*_{CO_2,model}\right)' \Sigma^{-1} \left(q^*_{CO_2,exp} - q^*_{CO_2,model}\right) \\ & s.t. \\ & f(\mu,\eta,\theta) = 0 \\ & g(\mu,\eta,\theta) \leqslant 0 \end{aligned} \tag{20}$$

Here, $q^*_{CO_2,exp}$ represents the experimental equilibrium loading of CO_2, $q^*_{CO_2,model}$ represents the equilibrium loading of CO_2 predicted by the chemistry model, θ represents the vector of estimated parameters, and $f(\mu,\eta,\theta)$ and $g(\mu,\eta,\theta)$ represent the equality constraints and inequality constraints of the model, respectively. Additionally, μ represents model inputs such as temperature and pressure, and η represents model variables such as mole fractions. In this problem, the equality constraints consist of the chemistry model equations, and the inequality constraints consist of variable bounds along with any additional constraints. This parameter estimation problem uses a least-squares type estimator with weighting function Σ^{-1}, which takes into account the uneven number of data points at low partial pressures of CO_2 and low temperatures. A similar method and weighting function was used by the authors in previous isotherm model development (Hughes et al., 2021). The model is implemented in Pyomo (Hart et al., 2017), a python-based software developed for optimization, and is solved using the interior point optimization algorithm IPOPT (Wächter and Biegler, 2006).

To evaluate the optimal combination of N and M, an information criterion was used to evaluate the tradeoff between the increasing model size and decreasing prediction error. Here, the Akaike Information Criterion (AIC) (Akaike, 1974) was used, shown in Eq. (21).

$$\text{AIC} = 2p + N_D \cdot \ln\left(\frac{obj}{N_D}\right) \tag{21}$$

Here, p is the total number of parameters and N_D is the total number of data points used for estimation.

2.2.1. Model reformulation

The chemistry model, as written above, contains several structural issues that present problems in the optimization solver and can result in poor convergence. First, the highly nonlinear solid–vapor equilibrium and reaction equilibrium equations can be difficult to converge. Second, the mole fraction variables for the chemisorption products are bounded between 0 and 1, and the value of these variables are expected to be at the lower bound when the CO_2 loading is low, which can cause issues with convergence of NLP solvers, especially interior points solvers. To address this challenge, a log transformation of the model was performed; the resulting improvements to the model structure are two-fold. First, the highly nonlinear solid–vapor equilibrium and reaction equilibrium equations are replaced by linear equations. Second, mole fraction variables in the transformed model are replaced by a new variable $\mathbb{Z}_i$, which does not need to satisfy the lower bound. This bound removal reduces the number of inequality constraints in the NLP problem, reducing its size, but most importantly removes the issue of the mole fraction variables converging near the lower bound of 0. A step-by-step derivation of the log transformed equations can be found in the Appendix.

2.3. Moving bed contactor model

The moving bed technology was initially used in drying processes, but has garnered attention in many industries, most notably in the petrochemical industry (Shirzad et al., 2019). Some of the earliest mathematical models of the moving beds were developed for coal gasifiers (Denn et al., 1979; Yoon et al., 1979a, 1979b, 1978), and some of the authors of this paper previously presented a model of a moving bed process for CO_2 capture using a functionalized sorbent (Kim et al., 2016). There exist other works in the literature, experimental and computational, that have demonstrated the potential of the moving bed process for carbon capture directly, such as by using a sorbent, or indirectly, such as through chemical looping combustion (Kim et al., 2016, 2013; Knaebel, 2009; Ku et al., 2014; Mondino et al., 2020, 2017; Morales-Ospino et al., 2021; Okumura et al., 2014; Ostace et al., 2018).

The moving bed model developed in this work closely follows the model developed by Kim *et al.* (Kim et al., 2016) and was implemented in Aspen Custom Modeler, which contains a framework that simultaneously solves the set of equations comprising mass, momentum, and energy conservation. The model is dynamic, nonisothermal, assumes spherical particles, and considers axial variation of the transport variables. Similar to previous modeling studies of post-combustion capture (Hughes et al., 2021; Kim et al., 2016; Kotamreddy et al., 2019), the moving bed contactor model includes a shell-and-tube type embedded heat exchanger to supply (remove) heat to (from) the system. The moving bed model was developed with the following key assumptions: (1) the distribution of process variables is axial; (2) particles flow uniformly throughout the bed with constant voidage and velocity; (3) there is no radial variation due to particle distribution; (4) there is no temperature variation within the particle; (5) particle attrition is negligible, and (6) the particles are 100% MOF (no binder).

The model also considers external and internal mass transfer limitations and heat transfer between the gas phase, solid phase, and embedded heat exchanger. The model also assumes that CO_2 is the only adsorbing species and the presence of other species in the flue gas do not affect the mass transfer of CO_2, which is an assumption that has been used in previous modeling studies for dmpn–Mg_2(dobpdc) (Hughes et al., 2021). This is a reasonable assumption based on available data for the uptake of select flue gas components in amine-appended

Mg_2(dobpdc). For example, previous work has shown that adsorption of O_2 and N_2 in dmpn–Mg_2(dobpdc) is negligible, and based on experimental breakthrough data, the material CO_2 capacity changed very little when exposed to dry and humid 15% CO_2 (balance N_2) (Milner et al., 2017). Additionally, as noted in the introduction, the same study showed that over the course of 1000 adsorption/desorption cycles with humid 15% CO_2 in N_2, the material achieves a stable cycling capacity. Additionally, a recent preliminary study of the stability of diamine-appended Mg_2(dobpdc) variants to SO_2—including dmpn–Mg_2(dobpdc)—suggests that these materials may also achieve high, stable CO_2 cycling capacities in the presence of this minor impurity (Parker et al., 2022). Finally, given the negligible uptake of O_2 and N_2 in the material, these gases are not expected to impact not have a significant effect on material regeneration or the energetics of CO_2 adsorption (Hughes et al., 2021).

2.3.1. Bulk Gas-Phase species balance

$$\varepsilon_b \frac{\partial C_{g,i}}{\partial t} = \varepsilon_b D_z \frac{\partial^2 C_{g,i}}{\partial z^2} - \frac{\partial \left(v_g C_{g,i}\right)}{\partial z} - (1-\varepsilon_b)\rho_p \frac{\partial Q_i}{\partial t} \tag{22}$$

In the gas-phase species balance presented in Eq. (22), ε_b represents the voidage in the bed, $C_{g,i}$ represents the concentration of species *i*, D_z is the effective axial dispersion coefficient, v_g is the superficial gas velocity, ρ_p is the particle density, and $\partial Q_i/\partial t$ is the rate of mass transfer between the gas phase and solid particles.

In this work, the Peclet number (Pe') is used for calculating the effective axial dispersion coefficient (Eq. (23)).

$$\frac{1}{Pe'} = \frac{D_z}{v d_p} = \frac{20}{Re_p Sc_p} + \frac{1}{2} \tag{23}$$

Here, v is the particle velocity and Re_p and Sc_p are the particle Reynolds and Schmidt numbers, respectively.

2.3.2. Solid-phase species balance.

$$(1-\varepsilon_b)\rho_p \frac{\partial q_i}{\partial t} = J_s \frac{\partial q_i}{\partial z} + (1-\varepsilon_b)\rho_p \frac{\partial Q_i}{\partial t} \tag{24}$$

The solid phase species balance is given by Eq. (24), where q_i is the particle loading of species *i*, and J_s is the solid flux (assumed to not vary with axial position in this work).

2.3.3. Mass transfer

The rate of the molar amount of CO_2 (Q_{CO_2}) transferred between the gas and solid phase is assumed to be the sum of the molar quantity of chemisorbed species ($q_{CO_2,chem}$) and phyisorbed species ($q_{CO_2,phys}$) and is given below:

$$\frac{dQ_{CO_2}}{dt} = \frac{dq_{CO_2,chem}}{dt} + \frac{dq_{CO_2,phys}}{dt} \tag{25}$$

$$\frac{dq_{CO_2,chem}}{dt} = k_{OC}\left[q^*_{CO_2,chem} - q_{CO_2,chem}\right] \tag{26}$$

$$\frac{dq_{CO_2,phys}}{dt} = k_{OP}\left[q^*_{CO_2,phys} - q_{CO_2,phys}\right] \tag{27}$$

Here, k_{OC} and k_{OP} are the overall mass transfer coefficients for spherical MOF pellets that account for particle diffusion and adsorption kinetics and have been developed previously using experimental thermogravimetric analysis and fixed bed breakthrough data (Hughes et al., 2021). Mass transfer coefficient equations and parameters can be found in the Appendix. $q^*_{CO_2,chem}$ and $q^*_{CO_2,phys}$ are the equilibrium loadings of the chemisorbed and physisorbed species, respectively, predicted by the chemistry model as discussed in Section 2.1.3.

The rate of adsorption/desorption in an adsorbent particle is calculated assuming a linear driving force:

$$R_i = \frac{6k_{f,i}}{d_p}\left(C_{g,i} - C_{surf,i}\right) = \rho_p \frac{\partial Q_i}{\partial t} \tag{28}$$

where $k_{f,i}$ is the external (gas film) mass transfer coefficient and $C_{surf,i}$ is the concentration of the gas at the particle surface. Eq. (28) determines $C_{surf,i}$ and accounts for any external mass transfer resistance across the gas film that surrounds the particle.

2.3.4. Energy balances

$$\varepsilon_b \rho_g C_{p,g} \frac{\partial T_g}{\partial t} = -\rho_g C_{p,g} v_g \frac{\partial T_g}{\partial z} - P\frac{\partial v_g}{\partial z} - (1-\varepsilon_b) a_p h_{gs}\left(T_g - T_s\right) \tag{29}$$

The gas-phase energy balance is given in Eq. (29). Here, T_g represents the temperature of the gas phase, $C_{p,g}$ is the heat capacity of the gas phase, a_p is the specific particle surface area, and h_{gs} is the heat transfer coefficient between the gas phase and the solid phase.

$$(1-\varepsilon_b)\rho_s C_{p,s} \frac{\partial T_s}{\partial t} = C_{p,s} J_s \frac{\partial T_s}{\partial z} + (1-\varepsilon_b) a_p h_{gs}\left(T_g - T_s\right) + \frac{\pi D_t N_{tube}}{A_{bed}} h_t (T_w - T_s) + \Delta H_{CO_2} \rho_s \frac{\partial Q_{CO_2}}{\partial t} \tag{30}$$

The solid-phase energy balance is given in Eq. (30). Here, N_{tube} is the number of heat exchanger tubes in the moving bed reactor, h_t is the heat transfer coefficient between the solid phase and heat exchanger tube wall, and T_w is the temperature of the tube wall. The last term in the solid phase energy balance accounts for the adsorption heat where ΔH_{CO_2} is the heat of adsorption.

The energy balance across the tube wall gives the following equation:

$$\pi(d_t - 2w_{thx}) N_{tube} h_{wgt}(T_w - T_{tube}) - \pi d_t N_{tube} h_t (T_w - T_s) = 0 \tag{31}$$

The energy balance for the tube side fluid is written in terms of enthalpy and is shown in Eq. (32).

$$F_t \frac{\partial H_t}{\partial z} - \pi(d_t - 2w_{thx}) N_{tube} h_{wgt}(T_w - T_{tube}) = 0 \tag{32}$$

Here, F_t is the flow of the tube side fluid, H_t is the enthalpy of the tube side fluid, and h_{wgt} is the heat transfer coefficient between the tube fluid and the inner side of the tube.

2.3.5. Heat transfer coefficients

Heat transfer coefficients used are taken from Kim *et al.* (Kim et al., 2016) and are based on the modified surface renewal theory. The correlations have origins for fluidized bed contactor models (Baskakov et al., 1973; Chen et al., 2005; Ruthven, 1984), but Kim *et al.* (Kim et al., 2016) have applied them to a moving bed model. The complete list of the heat transfer coefficient equations can be found in the Appendix.

2.3.6. Auxiliary equations

The behavior of a falling particle in the moving bed can be estimated by analogy to a fluidized bed. For maintaining the solid particles in the moving bed flow regime, the internal gas velocity through the bed should be less than the minimum fluidization velocity, v_{mf}, given by the equation below from Kunii and Levenspiel (Kunii and Levenspiel, 1991).

$$\frac{1.75}{\psi \varepsilon_{mf}^3}\left(\frac{d_p u_{mf} \rho_g}{\mu_g}\right)^2 + \frac{150(1-\varepsilon_{mf})}{\psi^2 \varepsilon_{mf}^3}\left(\frac{d_p u_{mf} \rho_g}{\mu_g}\right) = \frac{d_p^3 \rho_g (\rho_s - \rho_g) g}{\mu_g^2} \tag{33}$$

Therefore, the following constraint is satisfied at all positions in the bed.

$$v_g < v_{mf} \tag{34}$$

The embedded heat exchanger modeled in this work considers a trian-

gular tube pitch arrangement and the configuration is calculated using Eqs. (35) and (36) (Kakac et al., 2012).

$$N_t = (CTP)\frac{\pi D_b^2}{4A_1} \tag{35}$$

$$A_1 = (CL)P_t^2 \tag{36}$$

Here, D_b is the reactor diameter, N_t is the total number of tubes present in the reactor, A_1 is the cross-sectional area of a repeating unit in the reactor that contains a single tube, and P_t is the tube pitch. CTP and CL are the tube count calculation constant and the tube layout constant, respectively; for one tube pass, CTP=0.93 and CL=0.87 for 30 and 60 equilateral tri pitch. The same configuration has been used in previous modeling studies (Hughes et al., 2021; Kim et al., 2016; Kotamreddy et al., 2019).

2.4. Plant-wide model of the moving bed TSA process

A plant-wide model of the moving bed-based CO_2 adsorption/desorption process (see Fig. 1) model was developed in Aspen Custom Modeler v9. In the post combustion capture process, the MOF adsorbs CO_2 at near ambient conditions in the adsorber. As highlighted in the thermal management study in our previous work, removal of heat generated upon CO_2 adsorption is necessary to maximize the material adsorption performance (Hughes et al., 2021). Therefore, cooling water is used in the embedded heat exchanger of the moving adsorber to minimize increases in temperature. Following CO_2 adsorption, the cleaned flue gas is vented to the atmosphere and the CO_2-rich adsorbent particles are sent to the desorber. Before the particles enter the desorber, they are heated in the pre-heat exchanger, which uses sensible heat from the lean sorbent to heat the particles to regeneration conditions. This sensible heat recovery is an additional advantage of the moving bed process when compared to a fixed bed process. Steam is injected at the bottom of the desorber to aid in the removal of CO_2 from the reactor as well as reduce the partial pressure of CO_2 in the bed to aid in the driving force for mass transfer. Once the particles are regenerated in the desorber, they pass through the opposite side of the pre-heat exchanger to recover the heat and then are sent back to adsorber.

A key assumption in the process is that a single desorber does not necessarily have to process the same quantity of solids that passes through a single adsorber. For reactors of the same size and configuration, the desorber is frequently able to process more solids than the adsorber, largely because it operates at a higher temperature that enhances reaction rate constants and mass and heat transfer coefficients, thus resulting in a lower number of desorber beds needed for the system. Here, the solids flow to each contactor was set to achieve design conditions for CO_2 capture (adsorber solids flow) and lean loading (desorber solids flow). In order to avoid transitioning into a fluidized bed regime, the maximum gas velocity in moving beds is limited; this factor, in combination with the maximum size limitation of a single moving bed reactor, often necessitates the use of more than one moving bed to process the flue gas from commercial scale power plants. To size the process for industrial capture, the moving adsorbers were assumed to operate in parallel with the number of required beds, which was calculated based on the total flue gas flow rate from the power generation source and the design flow rate to a single bed. Similarly, the desorbers could operate in parallel, as needed, to regenerate the total amount of solids used in the adsorbers. The process was sized to capture CO_2 from an industrial size coal-fired power plant with total flue gas flow and composition taken from the baseline study published by the National Energy Technology Laboratory (Fout et al., 2015).

2.5. Cost model

The cost model here closely follows that used in our prior work (Hughes et al., 2021) and is briefly summarized here. Equipment costs were determined using Aspen Process Economic Analyzer (APEA). The moving bed reactors were costed as shell and tube heat exchangers due to their similar configuration and were scaled to the required size using economy of scale. In addition to the costing model presented in Hughes et al. (Hughes et al., 2021), three components are included here, which are the capital cost of the distributors within the moving bed, the capital cost of the cross heat exchanger, and the power required to circulate the solids using bucket elevators. The equations for these components along with the costing constants are taken from Kotamreddy (Kotamreddy, 2021) and are given in Eqs. (37) through (39).

$$A_{CEX} = \frac{Q_{CEX}}{U_{CEX}\Delta T_{LM}} \tag{37}$$

$$Cost_{dist} = 125\pi/4)(3.281{\cdot}D_b)^2 \tag{38}$$

$$P_{BE} = 6.88e^{-4}{\cdot}\dot{V}_{BE}{\cdot}(3.28{\cdot}D_H + 10){\cdot}DSF \tag{39}$$

Here, the capital cost of the cross exchanger is determined by its required heat transfer area (A_{CEX}). The cross exchanger is not rigorously simulated, and the heat transfer area is estimated using Eq. (37), which is then used to cost the exchanger using the same method as the moving bed reactors. The cost of a distributor for a single reactor is shown in Eq. (38) and calculated based on the diameter of the reactor. The power required by the bucket elevators (P_{BE}) is calculated using Eq. (39). The power is given in kilowatts and is a function of the solid volumetric flowrate in m^3/hr. The discharge height is in meters, and the drive safety factor (*DSF*), which varies depending on the class of the drive, is taken to be the upper bound of 2 in this work. Bare module capital costs are calculated by multiplying the purchased cost of the equipment by a factor to account for additional expenses due to labor, installation, overhead, and transportation (Turton et al., 2018). Additionally, the discount rate (or interest rate) is assumed to be 10% and the lifespan of the equipment is set to be 10 years. Operating costs of the process are calculated based on utility prices (see Table A1 in the Appendix) and usage, which is obtained from the moving bed process model simulations. The equivalent annual operating cost (EAOC) was then calculated using Eq. (40).

$$\text{EAOC} = \text{capital cost}\frac{\text{discount rate}}{\left(1-(1+\text{discount rate})^{-\text{number of years}}\right)} + \text{yearly operating costs} \tag{40}$$

The EAOC of a conventional post-combustion capture system using monoethanolamine (MEA) is used for comparison below and is taken from our prior work (Hughes et al., 2021), where it was calculated using results from a published study from the National Energy Technology Laboratory (Fout et al., 2015).

2.6. Technoeconomic optimization

The moving bed techno-economic optimization problem is given in Eq. (41). The goal of the optimization problem is to minimize the economic objective function, $f(x) = EAOC$, by optimizing the set of decision variables, denoted as x, which include design variables and operating conditions of the moving bed capture process.

$$\begin{aligned} &\min_x \; f(x) = EAOC \\ &s.t. \\ &h(x) = 0 \\ &g(x) \le 0 \\ &x^L \le x \le x^U \end{aligned} \tag{41}$$

The optimization problem is subject to equality and inequality con-

straints, denoted as $h(x)$ and $g(x)$, respectively. Here, the equality constraints consist of the rigorous, first-principles model equations of the moving bed process. The optimization problem is solved with the use of the FOQUS toolset (Miller et al., 2017), which is able to connect modeling platforms to numerous mathematical tools, including derivative free optimization algorithms. At each iteration of the derivative-free optimization algorithm, the FOQUS toolset will input the decision variables to the moving bed process model in Aspen Custom Modeler, run the model, and collect the results needed to calculate the economic objective function. This is a feasible path approach where the equality constraints of the optimization problem are satisfied at every iteration. In this work, the BOBYQA algorithm (Powell, 2009) is used to solve the optimization problem.

Eqs. (42) through (46) show design constraints and inequality constraints implemented in the moving bed optimization problem. The lean solids flow rate to the adsorber is calculated to achieve 90% capture of the CO_2 in flue gas feed, as shown in Eq. (42). The desorber solids inlet temperature is calculated based on the temperature approach design constraint shown in Eq. (43). Additionally, no trim heaters or coolers are considered, and the adsorber solids inlet temperature is calculated by solving the energy balance around the cross exchanger. For both the adsorber and desorber, the maximum gas velocity is constrained to be less than or equal to 85% of the minimum fluidization velocity as shown in Eqs. (44) and (45) to keep the process in the moving-bed regime. As the velocity is calculated at every axial position, this constraint is ensured along the entire length of the reactor. Lastly, the purity of the regenerated CO_2 stream leaving the top of the desorber was constrained to be greater than 95%.

$$CO_2 \text{ Capture Rate} = 90\% \tag{42}$$

$$\text{Cross Exchanger Temperature Approach} = 10\ ^\circ\text{C} \tag{43}$$

$$v_{g,ads} \leq 0.85 u_{mf,ads} \tag{44}$$

$$v_{g,des} \leq 0.85 u_{mf,des} \tag{45}$$

$$CO_2 \text{ Purity (mole basis)} \geq 95\% \tag{46}$$

The cost to produce MOF particles on an industrial scale is still not well known, and therefore multiple optimization runs were carried out using different estimates of adsorbent cost and particle lifespan. In particular, MOF prices of 0.5, 5, 15, and $30/kg were used based on the literature review performed in our previous economic modeling studies (Hughes et al., 2021). In this review, $0.5/kg was identified as a price for a well-established physisorbent but may be too low for amine-appended MOFs, and, in the authors' opinion, $5/kg is a more realistic lower bound. For particle lifespan, values of 0.5 and 2 years were used. There is little data available to support either of these assumed time periods for lifespan range, but these values are similar to that used in a solid sorbent direct air capture report published by NETL (0.5 years) (Valentine et al., 2022). Typical particle deactivation in fixed bed systems is due to irreversible reaction with contaminants in the flue gas, but the circulation of adsorbent solids in a moving bed can reduce the lifespan of the particles even further. In all, eight optimization scenarios were considered with differing combinations of MOF price and lifespan (see Appendix Table A2).

3. Results and discussion

3.1. Chemistry model

3.1.1. Reaction set selection

We first discuss the results for the reaction set selection and parameter estimation problems. The optimal set of formation reactions (i.e., values of N and M) was determined by solving the parameter estimation subproblem for multiple reaction sets and evaluating which combination minimizes the AIC (refer to Eq. (21)). The reaction sets were generated by taking possible combinations of N and M and include the smallest possible model with the least number of parameters—in other words, a scenario where only one chemisorption product is formed in a single formation reaction. This latter case was considered for completeness, but, as noted above, analysis of CO_2 uptake in dmpn–Mg_2(dopbdc) using solid-state ^{13}C NMR spectroscopy revealed that at low pressures, CO_2 adsorbs to form both the mixed product (as the major species) and ammonium carbamates that are not interacting with carbamic acids (as the minor species), and thus scenarios where both N and M are non-zero are expected to afford better models of the isotherm data.

The results of this analysis are shown in Fig. 2, and a complete list of the number of parameters, objective function value, and AIC for each model is given in Table A3. Notably, for all combinations of N and M, the AIC values are superior to that determined for the dual-site Sips isotherm model previously used by us to model the CO_2 adsorption data for dmpn–Mg_2(dobpdc) (Hughes et al., 2021). Here, the combination N=2 and M=1 yielded the lowest AIC value of −3418, which is nearly 42% lower than the value determined for the dual-site Sips isotherm model. As seen in Fig. 2, smaller models were associated with larger (less negative) AIC values, and they also yielded a less satisfactory fit to the experimental data; in contrast, larger models gave good fits to the experimental data, as shown by the objective function values in Table A3, but were associated with slightly larger AIC values due to the increased number of parameters.

3.1.2. Parameter estimation and validation

In Fig. 3, experimental CO_2 adsorption isotherms for dmpn–Mg_2(dobpdc) are plotted together with the optimal reaction model. It is clear that the chemistry model is able to accurately represent the experimental data at all temperatures and across the experimental pressure range, and when compared to the Sips isotherm model developed previously (Hughes et al., 2021), the chemistry model performs better at high partial pressures. The objective function value (as calculated by Eq. (20)) for the chemistry model is also nearly six times less than that for the Sips model (1.69 versus 9.48 $[mol/kg]^2$, respectively; see Table A4 for a complete list of the estimated parameters for the optimal chemistry model).

The chemistry model was also evaluated by investigating how well it predicts validation data that were not a part of the parameter estimation data set—here, adsorption isotherm collected at 80 and 90 °C. Fig. 4 shows that the chemistry model is able to predict the validation data reasonably well. At 80 °C, the model predicts a less sharp adsorption step than the experimental data, similar to what is seen for the model at 75 °C in Fig. 3. An important feature of the data that a model should capture is the position of the step transition for a specific temperature. The model shows a step transition at 80 °C centered around ~4e+4 Pa which is consistent with the experimental data. The step transition predicted by the model isn't quite as steep as the data shows, but the model still predicts this well. In contrast, at 90 °C both the model and the data do not exhibit a step-transition in the pressure range for which the data was collected. The model predicts a slightly higher uptake in the mid-pressure region than is observed experimentally, while this difference is more pronounced at higher pressures. The R^2 value of the validation data prediction is 0.93, which is 1% lower than the R^2 of the Sips Isotherm model (=0.94) for the same validation data set (Hughes et al., 2021). A visual comparison of the chemistry model vs. the Sips Isotherm model for the estimation data and validation data is included in the Appendix (see Fig. A1).

3.1.3. Heat of adsorption constraint

The heat of CO_2 adsorption, which is calculated using Eq. (19), was included as an inequality constraint in the model. Experimental data for the heat of adsorption is not available in the literature, and so the heat of adsorption versus loading reported by Milner et al. (Milner et al., 2017),

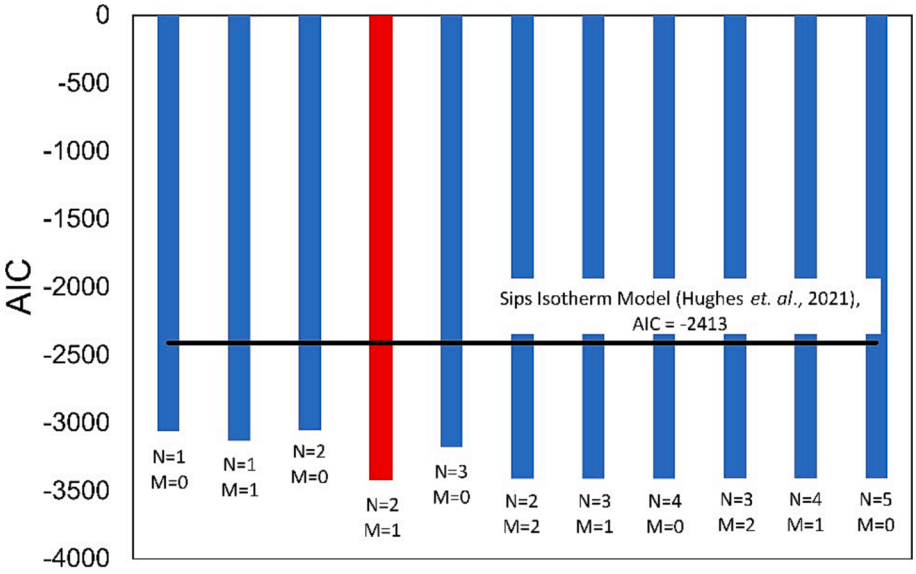

Fig. 2. Integer sensitivity results for model selection showing the AIC values generated for varying combinations of N and M. As noted in Section 2.1.2, because the formation reactions proposed here are equivalent as defined, an analogous figure generated with values of N and M swapped would be equivalent to the plot shown here. The lowest AIC value (−3418) was determined for N=2 and M=1 (red bar). Black line corresponds to Sips isotherm model from Hughes et al. (Hughes et al., 2021).

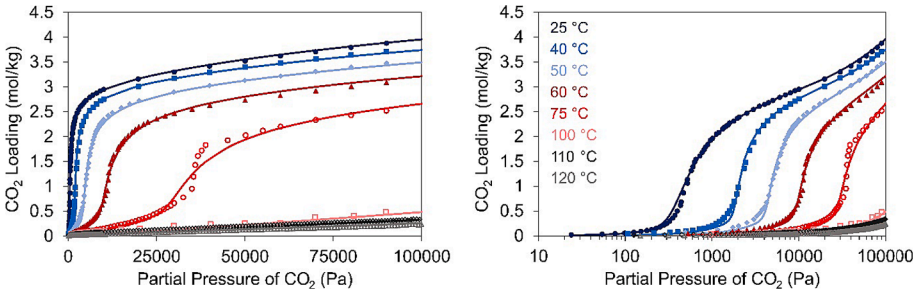

Fig. 3. Parameter estimation results for N=2 and M=1 for linear pressure scale (left) and logarithmic pressure scale (right). Symbols represent experimental data and lines represent model prediction.

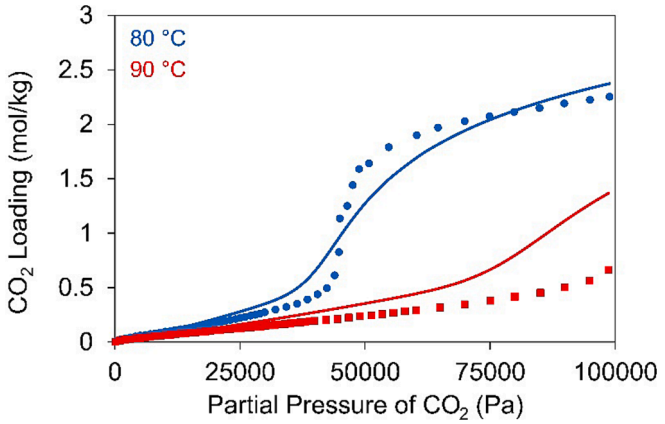

Fig. 4. Optimal chemistry model (N=2, M=1) prediction of validation data. Symbols represent experimental data and lines represent model prediction.

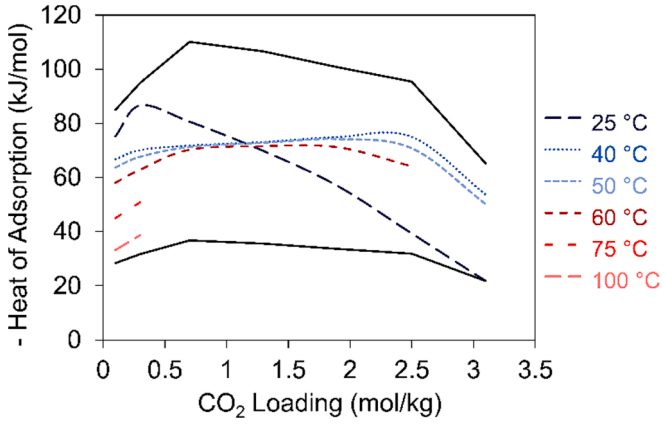

Fig. 5. Chemistry model heat of adsorption as a function of loading and temperature. Solid black lines represent the upper and lower bounds, and dashed lines represent model prediction at different temperatures.

which was calculated using the Clausius–Clapeyron equation, was taken as a baseline. Using this, a constraint which ensures that the heat of adsorption predicted by the model is within ± 50% of the baseline data from Milner *et al.* (Milner et al., 2017) was included in the NLP parameter estimation problem. To avoid adding a large number of equations to the parameter estimation problem, the heat of adsorption was calculated at only a few representative CO_2 loadings for each temperature, rather than every experimental isotherm data point. Fig. 5 shows the heat of adsorption predicted by the chemistry model at

temperatures ranging from 25 to 100 °C as well as the upper and lower bounds implemented as an inequality constraint based on the data from Milner et al. (Milner et al., 2017). The predicted heats of adsorption at 40, 50, and 60 °C correspond closely with the baseline value over the entire range of loadings examined and are well within the upper and lower bounds. However, at 25 °C the model overestimates and underestimates the heat of adsorption at low and high loadings, respectively, and at a loading of 3.1 mol/kg, the model isosteric heat lies on the lower bound. Finally, the predicted heats of adsorption at 75 and 100 °C are lower than the baseline but still well above the lower bound. It should also be noted that the baseline taken from Milner *et al.* (Milner et al., 2017) was calculated by assuming the heat of adsorption does not vary with temperature, and therefore variations when examining a single temperature can be expected. Still, ensuring that the heat of adsorption is within a practical and expected range for the MOF system can help avoid overfitting to experimental data.

3.1.4. Chemisorption reactant and product loadings

Thus far we have focused on how well the model predicts the total CO_2 loading of the system as well as the heat of adsorption. However, analyzing the contribution of individual species is valuable and can be important in identifying species or reaction pathways, but this is impossible for many of the heuristic isotherm models, as they do not model these species or go into this type of resolution. In this section, the profiles for the optimal chemistry-based model are presented and analyzed.

Fig. 6 shows the loadings for the two main reactants involved in CO_2 chemisorption, namely the diamine and free CO_2. At very low partial pressures of CO_2, the loading of amine converges to the total amine loading (Q_{Am}) in pristine dmpn–Mg_2(dobpdc) (3.82 mol/kg), which is expected given that no CO_2 will be adsorbed as the partial pressure nears zero (Fig. 6a). At the lowest three temperatures considered (25, 60, and 75 °C), the change in the amine loading exhibits a step-shaped profile with respect to partial pressure, with step positions at each temperature consistent with the step positions in the corresponding CO_2 isotherm data. In contrast, for the highest two temperatures of 100 and 120 °C, the loading decreases only slightly in a linear fashion, consistent with a small amount of CO_2 uptake in the pre-step region that is relevant at these temperatures and pressures. Fig. 6b shows that the free CO_2 is present in only very small amounts across the entire temperature and pressure range considered. At 25 °C, this CO_2 contributes almost negligibly to the total CO_2 loading because it is consumed during chemisorption. At 60 and 70 °C, there is a slight increase in the loading of this free CO_2 at low pressures before the respective adsorption step threshold pressures are achieved, and then the loading gradually levels off. At the highest two temperatures, the loading steadily increases, again consistent with a low uptake in the pre-step region before chemisorption.

Fig. 7a shows the total amount of chemisorbed CO_2 loaded in the material, as predicted by the optimal chemistry model for select temperatures and pressures ranging from 0 to 1 bar. At 25, 60, and 75 °C the model predicts a step-shaped increase in the loading of chemisorbed CO_2; the loading at each temperature also plateaus at a value very close to the CO_2 loading measured experimentally at the top of the step (i.e., before the onset of more gradual uptake) in the corresponding adsorption isotherms. These data indicate that chemisorbed CO_2 is the main contributor to the step-shaped CO_2 adsorption profile for dmpn–Mg_2(dobpdc) at these temperatures. Above 75 °C, the loading of chemisorbed CO_2 is negligible over the entire pressure range, consistent with the absence of stepped CO_2 adsorption at these those temperatures.

Fig. 7b shows the percentage of chemisorbed CO_2 that is incorporated as product B_i, formed in the first chemisorption reaction defined above (in N=2 reaction steps). Interestingly, the majority of the chemisorbed CO_2 (≥80%) is present in this single product at 25, 60, and 75 °C and pressures above the experimental threshold pressure for CO_2 adsorption at each of these temperatures. In contrast, at these temperatures the second chemisorbed species (C_i) dominates only at very low partial pressures before the onset of stepped adsorption. This distribution of chemisorption products is consistent with prior solid-state ^{13}C NMR spectroscopy data collected for CO_2 loading in dmpn–Mg_2(dobpdc), which found that a minor chemisorption product consisting of ammonium carbamates (here, product C_i) is formed at low pressures, whereas the mixed chemisorption product is the sole product at higher pressures (here, product B_i) (Forse et al., 2018). At temperatures of 100 and 120 °C, for which there is no stepped CO_2 uptake up to 1 bar, most of the chemisorbed CO_2 is present as the second product species, C_i.

3.1.5. Chain lengths

The length of the main cooperatively adsorbed product chain was estimated as part of the parameter estimation problem solved in this work. McDonald et al. (McDonald et al., 2015) previously used the Hill equation (Weiss, 1997) to estimate the relative number of CO_2 molecules involved in cooperative ammonium carbamate chain formation in mmen–M_2(dobpdc) (mmen = *N,N′*-dimethylethylenediamine; M = Mg, Mn, Fe, Co, Ni, Zn). Table 1 compares the chain length estimated in this work for dmpn–Mg_2(dobpdc) and the Hill coefficients calculated for mmen-M_2(dobpdc). The value presented for this work is calculated by taking the sum of n_1 and n_2, and the Hill coefficients were calculated using only 25 °C isotherm data. Table 1 shows that the chain length estimated by this work are similar to those estimated previously for similar solid sorbents.

3.1.6. Physisorbed loading

Fig. 8a shows the predicted loading of physisorbed CO_2 in dmpn–Mg_2(dobpdc) over the experimental temperature and CO_2 pressure range. The physical adsorption in this case is not associated with stepped adsorption, and so was modeled using a standard Langmuir isotherm equation. Fig. 8b shows the percentage of total adsorbed CO_2 that is physisorbed in the material at different temperatures and pressures. At 25, 60, and 75 °C, the fraction of physisorbed CO_2 remains relatively low over the entire pressure range, given that the stepped CO_2 uptake at these temperatures accounts for the majority of adsorbed CO_2 (see Fig. 2). However, the amount of physisorbed CO_2 increases at higher pressures, corresponding to uptake in the post-step region at

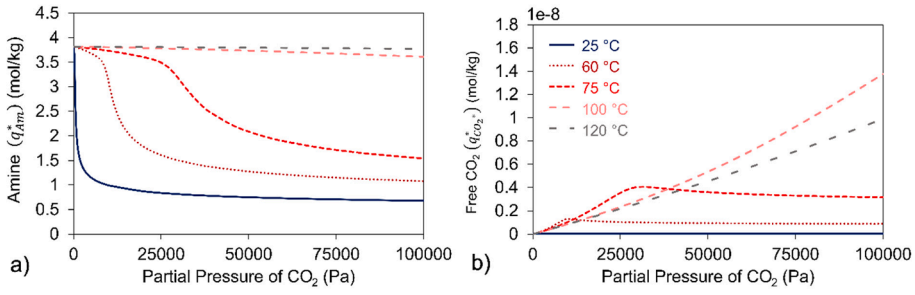

Fig. 6. Loadings [mol/kg] of the species present in the optimal chemistry model (N=2, M=1). a) Unreacted diamine (Am). b) Adsorbed phase free CO_2 (CO_2^*).

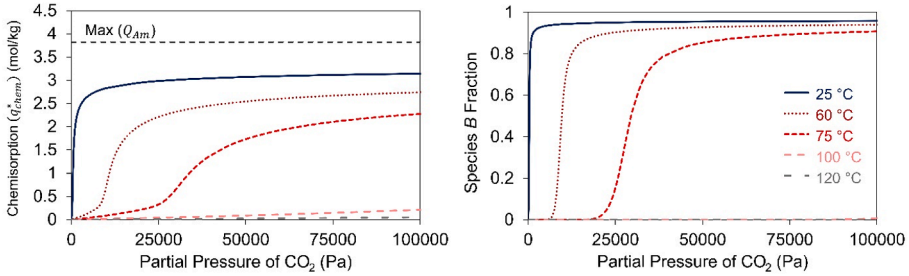

Fig. 7. Prediction of chemisorbed CO_2 loading and chemisorbed product distribution. Left) Total chemisorbed CO_2 loading. Dashed line represents the maximum achievable loading (Q_{Am}). Right) Fraction of chemisorbed CO_2 contained in chemisorbed species *B*.

Table 1
Comparison of chain length estimations for varying MOFs and methods.

MOF	Value	Method	Source
dmpn-Mg_2(dobpdc)	11.0	Chemistry Model	This work
mmen-Mg_2(dobpdc)	10.6	Hill Coefficient	(McDonald et al., 2015)
mmen-Mn_2(dobpdc)	5.6	Hill Coefficient	(McDonald et al., 2015)
mmen-Fe_2(dobpdc)	7.5	Hill Coefficient	(McDonald et al., 2015)
mmen-Co_2(dobpdc)	11.5	Hill Coefficient	(McDonald et al., 2015)
mmen-Zn_2(dobpdc)	6.0	Hill Coefficient	(McDonald et al., 2015)

these temperatures. At the two highest temperatures considered, for which there is no stepped adsorption observed experimentally, the majority of adsorbed CO_2 is predicted to be physisorbed in the material with the remaining adsorbed CO_2 existing as a chemisorbed product.

3.2. Techno-economic optimization of the moving bed TSA process

Fig. 9 shows estimated EAOC of the moving bed process for varying combinations of adsorbent price and lifespan. Unsurprisingly, the lowest EAOC ($128 million/year) is for Case 5, where the MOF price is the least expensive ($0.5/kg) and the lifespan is the longer of the two options, at two years. This EAOC is 49% less than that predicted for a conventional post-combustion capture system using monoethanolamine (Fout et al., 2015). Two of the cases considered here have larger EAOCs than the MEA process, namely Cases 3 and 4, for which the lifetime of the MOF is assumed to be only six months, and the cost of the particles are the two highest values at $15 and $30/kg, respectively. Case 3 is only slightly more costly than the MEA process, while Case 4 is 44% more costly ($362 million/year) and considered to be an extreme case and unlikely. Table 2 shows the results of the moving bed optimization problem for Case 1, including the design and operating variables that were considered as decision variables, their optimized values, and their lower and upper bounds. Table 3 shows the minimized EAOC for Case 1 along with a breakdown of the significant contributing costs. A complete list of optimized design variables and costing breakdown is included in the Appendix (see Table A5 and A6).

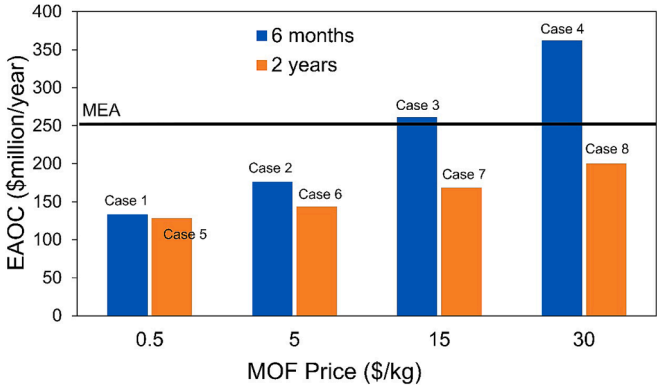

Fig. 9. MB optimization results for varying MOF price and lifespan.

Table 2
MB optimization results, Case 1.

Decision Variable	Optimized Value	Lower Bound	Upper Bound	Units
Adsorber Height	3.63	1	20	[m]
Adsorber Diameter	10	1	10	[m]
Adsorber Tube Pitch	0.082	0.035	0.5	[m]
Desorber Height	13.18	1	20	[m]
Desorber Diameter	10	1	10	[m]
Desorber Tube Pitch	0.114	0.035	0.5	[m]
Lean sorbent loading	0.388	0.025	1	[mol/kg]
Adsorber Outlet Pressure	1.01	1.01	2.0	[bar]
Flue Gas Flowrate to a single bed	2122	0	–	[kmol/hr]
Direct Steam Flowrate	97.6	0	–	[kmol/hr]

3.2.1. Moving bed profiles

Fig. 10 shows the axial profiles for important process variables, including gas phase composition, solids loading, and temperature. Coal

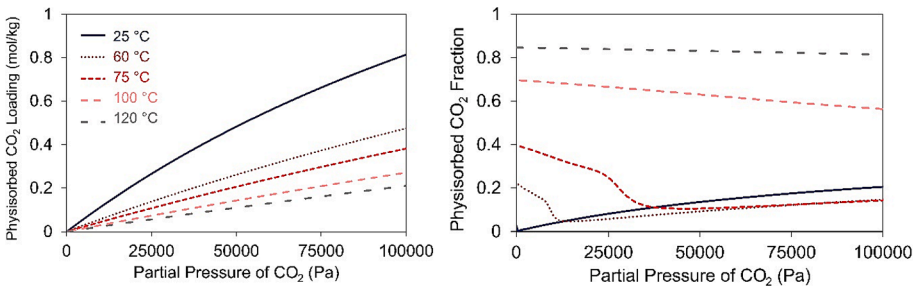

Fig. 8. (a) Prediction of the loading of physisorbed CO_2 in dmpn–Mg_2(dobpdc) at a range of temperatures and pressures. (b) Fraction of the total CO_2 loading which is physisorbed.

Table 3
Costing breakdown [$million/year] for Case 1 optimized moving bed capture process.

Amortized Capital	**30.43**
Reactors	20.83
Blowers	0.93
Cross Exchanger	8.67
Yearly Operating Costs	**102.84**
Steam	93.81
Electricity	2.96
Cooling Water	0.28
Sorbent	5.79
EAOC	**133.27**

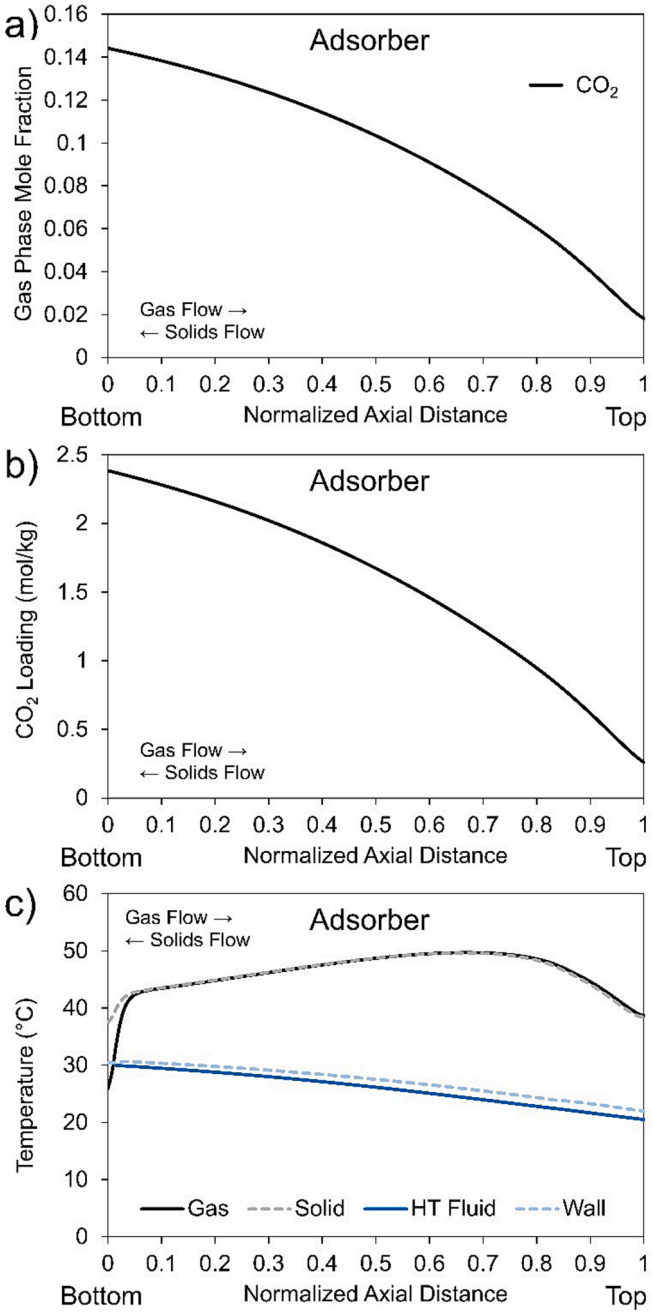

Fig. 10. Adsorber Moving Bed Profile Plots. a) Gas phase CO_2 mole fraction. b) Solids phase CO_2 loading. c) Temperature profiles for gas phase, solid phase, heat transfer fluid, and tube wall. X axis is normalized axial distance along the reactor with 0 being the bottom of the moving bed and 1 being the top.

flue gas entering the bed has a CO_2 concentration of 14.6% (v/v or mol %), and the quantity of CO_2 steadily decreases as the gas travels upwards through the bed and is captured by the adsorbent (Fig. 10a). Similarly, the loading of CO_2 in the adsorbent monotonically increases as the solid travels downward through the bed and captures CO_2 (Fig. 10b). The temperature profiles across the moving bed for the gas phase, solid phase, heat transfer fluid (cooling water), and tube wall are shown together in Fig. 10c. As the cooling water flows downward through the embedded heat exchanger and removes heat from the bed (refer to Fig. 1), it increases in temperature. The adsorbent likewise flows from the top to the bottom of the bed, and the temperature of the solid increases near the top of the bed as fresh, lean sorbent begins to quickly adsorb CO_2 and generate heat but remains somewhat constant in the remainder of the bed as the embedded exchanger and the cooling water are able to effectively remove the heat generated from adsorption. Additionally, since the dominating heat transfer occurs between the solid phase and the tube wall, the temperature of the gas phase quickly approaches that of the solid phase, and the two temperatures are nearly the same throughout the length of the bed.

Similarly, Fig. 11 shows the same axial profiles for the moving bed desorber. Pure steam is fed through the bottom of the desorber to aid in mass transfer by reducing the partial pressure of CO_2. However, the gas phase composition profile in Fig. 11a shows that the desorbed CO_2 quickly becomes the primary species in the gas phase. Note, the composition at the top of the desorber is 95% CO_2, which was included as a constraint in the techno-economic optimization problem. Fig. 11b shows the CO_2 loading profile of the adsorbent: the loading decreases as the solids flow downwards through the bed and CO_2 is desorbed. As shown in Fig. 11c, the temperature of the adsorbent initially decreases at the top of the desorber as heat is consumed to regenerate the solid. Solid that is further along in the adsorber and has been regenerated then begins to increase in temperature as it remains in contact with the steam and embedded heat exchanger. It should be noted that water condensation from the gas phase is not currently considered in the model, but there is a possibility this could occur based on the operating conditions of the desorber. For the optimal conditions presented in Fig. 11, the relative humidity at all points in the bed is $\ll 1$, so condensation is not expected but is something that should be monitored in any future designs.

3.2.2. *Capital cost uncertainty analysis*

A sensitivity study for the effect of capital cost uncertainty on overall process economics was performed. Here, the amortized capital cost for each case is multiplied by an assumed factor, ±50% is used in this study, to evaluate the effect on total process economics with results shown in Fig. 12. Separate trends are shown for each particle lifespan with the MOF price shown on the horizontal axis. Overall, the change is relatively small for each case with the largest change occurring for Case 4 which shows a change of 7% when this capital cost uncertainty is considered. The values presented in Fig. 12 are listed in Table A7.

3.2.3. *Comparison to fixed bed process*

As noted above, we previously presented a techno-economic analysis of a post-combustion capture process using dmpn–Mg_2(dobpdc) as the adsorbent in fixed bed contactors (Hughes et al., 2021). In that work, we performed an analogous sensitivity study examining the impact of the price of the MOF on the EAOC of the fixed bed process. Table 4 compares the results for that study to the optimized moving bed TSA process in this work. The cost of capture, a common costing metric for CO_2 capture systems, is also presented in Table 4, and is calculated by simply dividing the EAOC by the amount of CO_2 captured by the process in an entire year. When the same adsorbent lifespan and price is considered, the moving bed process significantly outperforms the fixed bed process. Even when a lifespan of only 6 months is considered for the adsorbent in the moving bed process, the economics of that process are more favorable than the fixed bed process, with equivalent MOF prices. It should be

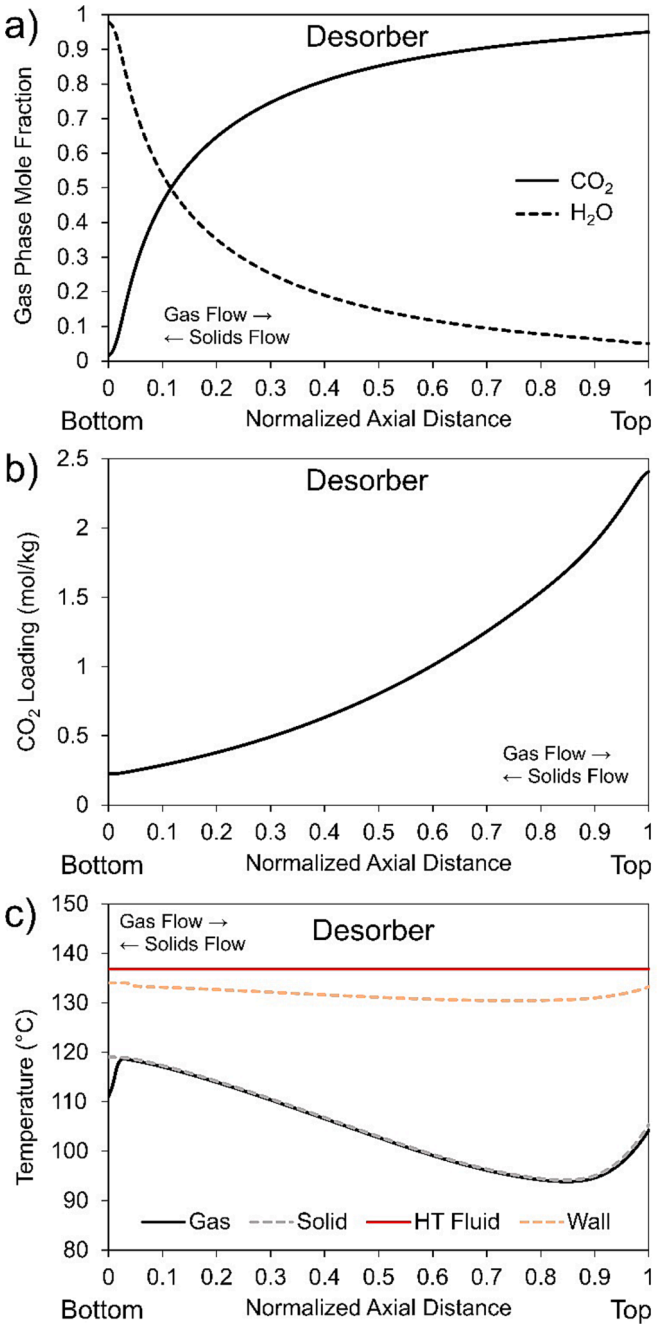

Fig. 11. Desorber Moving Bed Profile Plots. a) Gas phase CO_2 mole fraction. b) Solids phase CO_2 loading. c) Temperature profiles for gas phase, solid phase, heat transfer fluid, and tube wall.

noted that the economics of the fixed bed process were investigated using single-variable sensitivity studies and what was deemed a practical degree of heat recovery. However, if further process optimization were performed along with a detailed design of the heat recovery process, it is likely the economics would improve.

The reduction in EAOC of the moving bed process is due in large part to the reduction in amortized reactor capital and steam operating costs. The moving bed process is capable of much more compact reactors since adsorption and desorption are carried out in separate units, unlike the fixed bed process in which all steps occur in the same unit, and designs can target the limiting mechanisms for each step. As a result, the amortized reactor capital cost of all the moving bed cases (see Table A6) is nearly 4x lower than the fixed bed TSA process (~$25 million/year vs.

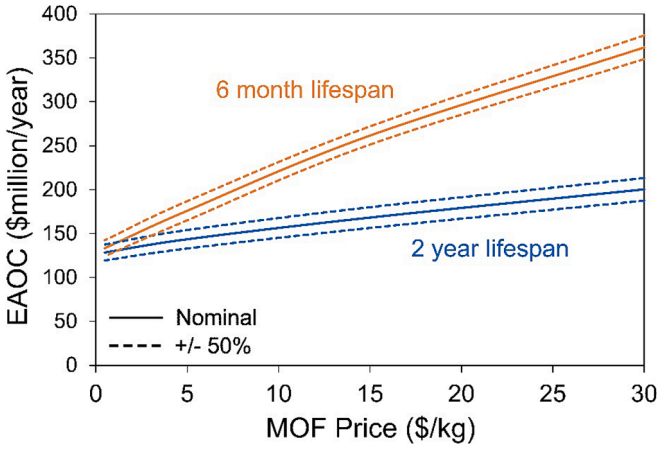

Fig. 12. Capital cost uncertainty analysis for optimal moving bed cases. Solid lines represent the nominal cases and dashed lines represent a +/- 50% change in amortized capital costs.

Table 4
EAOC and cost of capture values for varying MOF capture processes, lifespans, and prices.

dmpn-Mg_2(dobpdc) Capture Process	MOF Lifespan	MOF Price ($/kg)	EAOC ($million/year)	Cost of Capture ($/tonne)
Fixed Bed TSA, Practical Heat Recovery (Hughes et al., 2021)	2 years	0	251	62.7
		15	341.6	85.4
		30	427	106.7
Moving Bed TSA	2 years	0.5	128.4	32.1
		5	143.5	35.9
		15	168.1	42.0
		30	200.3	50.1
Moving Bed TSA	6 months	0.5	133.3	33.3
		5	175.8	43.9
		15	261.5	65.3
		30	362	90.5

$99 million/year (Hughes et al., 2021)). The thermal energy requirements, directly related to the steam operating costs, for the fixed bed process from our previous work and the moving bed process cases are shown below in Table 5. The values are calculated considering only the thermal energy supplied by steam, and the fixed bed value incorporates a practical heat recovery of 35% which lowers the value from the originally presented value of 3.23 (Hughes et al., 2021) to 2.62 MJ/kg CO_2. The energy requirements of the moving bed process vary slightly for each case due to the different operating conditions of each case found by the process optimization. The average value among all cases is 1.75 MJ/kg which is a 33% reduction from the fixed bed process and is also 17% lower than the value of 2.1 MJ/kg CO_2 presented by Milner *et. al.*

Table 5
Thermal energy requirements for fixed bed capture processes and the moving bed processes evaluated in this work.

dmpn-Mg_2(dobpdc) Capture Process	Thermal Energy Requirement [MJ/kg CO_2]
Fixed Bed TSA, Practical Heat Recovery (Hughes et al., 2021)	2.62
Moving Bed TSA	
Case 1	1.72
Case 2	1.75
Case 3	1.76
Case 4	1.79
Case 5	1.71
Case 6	1.73
Case 7	1.76
Case 8	1.77

(Milner et al., 2017) which assumes a theoretical temperature swing and working capacity. When compared to the theoretical values assumed by Milner *et. al.,* the moving bed process is nearly able to achieve the same working capacity (2.13 mol/kg for the moving bed vs. the theoretical 2.42 mol/kg) and requires a smaller amount of sensible heat (a 10 °C swing vs. a 60 °C theoretical swing) due to the large amount of heat recycled by the cross-exchanger. The high working capacity achieved by the moving bed process and large amounts of heat recycled by the cross-exchanger are responsible for the reduction in energy requirements.

4. Conclusions

A chemistry-based model is developed to describe the adsorption equilibrium of an amine-appended MOF, specifically dmpn-Mg_2(dobpdc), for the first time. Selection of the optimal cooperative adsorption reactions proposed in this work is performed based on exhaustive enumeration of combinations of integer variables for minimizing the AIC. The optimal reaction set is found to be: N=2 and M=1 which gives an AIC value of −3418 and is a reduction of nearly 42% when compared to the previously developed Sips isotherm model. The optimal reaction combination also gives an excellent fit to the experimental isotherm data, showing a nearly 6x reduction of the weighted least squares objective function used in this work when compared to the Sips isotherm model. The chemistry model also performs well when testing against a validation data set and gives chain length values that compare well to those estimated for other amine-appended MOFs. Overall, this model gives better prediction of the experimental data while giving an insightful look into the compositions of cooperatively adsorbed species and how they change with varying temperatures and pressures which has not been done for previous amine-appended isotherm models. In future, this model can be enhanced to provide a much better framework for incorporating interactions with other species, mainly water. Additionally, the uptake of water and how it affects CO_2 loading is an important area of future work for this model. The model can also be expanded to include enthalpy models which will give a better prediction of the heat of adsorption if experimental data becomes available. Evaluation of new materials by identifying limiting pathways can also be a focus of future work. The framework of this chemistry-based model also makes it generic enough to be applied to other functionalized sorbents which can be a focus of future work.

Techno-economic optimization, undertaken by developing a detailed plant-wide model of the MB-based adsorption/desorption process and a cost model, results in nearly 43% lower EAOC than the MEA baseline process when a MOF price of 5 $/kg and lifespan of 2 years is considered. With considerable advances being made in the manufacturing of the functionalized MOF sorbents and with large scale utilization of these materials, MOF particle lifespan is expected to go up and cost is expected to go down. If we consider the cost of MOF to be $15/kg and life span of 2 years (i.e., Case 7), which is the most likely scenario in the near future in the authors' view, EAOC offered by the diamine-appended MOF is about 33% lower than MEA. The moving bed process also shows a significant cost reduction for all cases investigated when compared to the fixed bed dmpn-Mg_2(dobpdc) TSA process which can be attributed to a reduction in capital cost (-75%) and energy requirement (–33%).

The studies completed in this work provide insight into the possible improvement in process economics that a MB process can provide when compared to a traditional solvent process and even other type of contactors for sorbent-based processes. Future work should focus on better understanding some of the areas of uncertainty that were investigated in this work, specifically the price of the MOF sorbent and lifespan of the particle as they have been shown to have a significant effect on the process economics. Additionally, the increased attrition of the MB process due to the circulation of the particles can decrease particle lifespan below the range which is even considered here. Investigation of the MOF particle attrition in a MB process would be needed before any real-world application. The adsorption of water and how it affects the energetics of the process and the costs to maintain the water balance should be investigated in future works. The gas velocity constraint required to keep the process in the MB regime results in a large number of adsorbers needed to process the flue gas due to the low volumetric flow rate to a single bed. An area of future would be investigating hybrid systems which use a MB contactor for regeneration and another type of solid contactor for adsorption, such as a fluidized bed.

5. Disclaimer

This project was funded by the Department of Energy, National Energy Technology Laboratory an agency of the United States Government, through a support contract. Neither the United States Government nor any agency thereof, nor any of its employees, nor the support contractor, nor any of their employees, makes any warranty, expressor implied, or assumes any legal liability or responsibility for the accuracy, completeness, or usefulness of any information, apparatus, product, or process disclosed, or represents that its use would not infringe privately owned rights. Reference herein to any specific commercial product, process, or service by trade name, trademark, manufacturer, or otherwise does not necessarily constitute or imply its endorsement, recommendation, or favoring by the United States Government or any agency thereof. The views and opinions of authors expressed herein do not necessarily state or reflect those of the United States Government or any agency thereof.

CRediT authorship contribution statement

Ryan Hughes: Conceptualization, Formal analysis, Methodology, Software, Writing – original draft. **Goutham Kotamreddy:** Conceptualization, Methodology, Writing – review & editing. **Debangsu Bhattacharyya:** . **Surya T. Parker:** . **Matthew N. Dods:** Data curation, Resources, Writing – review & editing. **Jeffrey R. Long:** Data curation, Resources, Writing – review & editing. **Benjamin Omell:** Funding acquisition, Project administration, Writing – review & editing. **Michael Matuszewski:** Funding acquisition, Project administration, Writing – review & editing.

Declaration of competing interest

The authors declare that they have no known competing financial interests or personal relationships that could have appeared to influence the work reported in this paper.

Data availability

All data used are for public domain that have been referenced.

Acknowledgements

We graciously acknowledge funding from the U.S. Department of Energy, Office of Fossil Energy and Carbon Management, through the Point Source Carbon Capture Program (DE-FE0025912). M.N.D. gratefully acknowledges support from a National Science Foundation Graduate Research Fellowship. S.T.P thankfully recognizes support from a NASA Space Technology Research Fellowship.

Appendix

A1. Methods: Chemistry Model Reformulation

First, the natural log was applied to the solid–vapor equilibrium equation.

$$ln\left(y_{CO_2}\widehat{\phi}_{CO_2}P\right) = ln\left(\gamma_{CO_2}\right) + ln\left(z_{CO_2^*}\right) + ln\left(f^0_{CO_2}\right) \tag{A1}$$

Substituting $\widehat{\phi}_{CO_2} = 1$ and $f^0_{CO_2} = k_{H,CO_2}$, Eq. (A1) becomes:

$$ln\left(y_{CO_2}P\right) = ln\left(\gamma_{CO_2}\right) + ln\left(z_{CO_2^*}\right) + ln\left(k_{H,CO_2}\right) \tag{A2}$$

Next, the natural log is applied to the reaction equilibrium equation.

$$ln\left(K_{eq}\right) = \sum_{i=1}^{J} v_i ln(z_i) \tag{A3}$$

This transformation results in new linear equations, but additional steps must be taken to avoid calculating the natural log in an equation-oriented framework. The LHS of the transformed SVE equation can be handled by a preprocessing of the experimental data and is simply a fixed input into the parameter estimation problem. The correlations for the activity coefficient of CO_2, Henry's constant, and the reaction equilibrium constant are already written for the natural log of each term and can simply be substituted into the equations. To address the natural log of mole fractions, a new transformed mole fraction variable, $\mathbb{Z}$, is introduced in Eq. (A4). Bound transformation for this new variable is also performed and shown in Eq. (A5).

$$z_i = exp(\mathbb{Z}_i) \tag{A4}$$

$$\mathbb{Z}_i \in [-\infty, 0] \tag{A5}$$

Substituting this new variable into Eqs. (A2) and (A3) yields the linear equations shown below.

$$ln\left(y_{CO_2}P\right) = ln\left(\gamma_{CO_2}\right) + \mathbb{Z}_{CO_2^*} + ln\left(k_{H,CO_2}\right) \tag{A6}$$

$$ln\left(K_{eq}\right) = \sum_{i=1}^{J} v_i \mathbb{Z}_i \tag{A7}$$

Substitution can also be performed for the remaining chemistry model equations in which mole fractions appear and are shown below for clarity.

$$\ln\left(\gamma_{CO_2}\right) = exp(\mathbb{Z}_{Am})\left[\tau_A - \tau_B\left(exp(\mathbb{Z}_{Am}) - 2exp\left(\mathbb{Z}_{CO_2^*}\right)\right)\right] - exp\left(\mathbb{Z}_{CO_2^*}\right)exp(\mathbb{Z}_{Am})\left[\tau_A + 2\tau_B\left(exp\left(\mathbb{Z}_{CO_2^*}\right) - exp(\mathbb{Z}_{Am})\right)\right] \tag{A8}$$

$$exp(\mathbb{Z}_{Am}) + exp\left(\mathbb{Z}_{CO_2^*}\right) + \sum_{j=1}^{N} exp\left(\mathbb{Z}_{B_j}\right) + \sum_{j=1}^{M} exp\left(\mathbb{Z}_{C_j}\right) = 1 \tag{A9}$$

$$q_i^* = Q^* exp(\mathbb{Z}_i) \tag{A10}$$

A2. Methods: Mass Transfer Coefficients

Equations to calculate the overall mass transfer coefficients for the chemisorption and physisorption species are shown in Eqs. (A11-A15). Equations and estimated parameters are taken from Hughes *et. al.* (Hughes et al., 2021). The equations consider a sum of resistances for particle diffusion and reaction kinetics to predict the overall mass transfer coefficient.

$$\frac{1}{k_{OC}} = \frac{r_p^2}{15\varepsilon_p D_{eff}} + \frac{1}{k_{chem}} \tag{A11}$$

$$\frac{1}{k_{OP}} = \frac{r_p^2}{15\varepsilon_p D_{eff}} + \frac{1}{k_{phys}} \tag{A12}$$

$$D_{eff} = C_1 (T_s)^{0.5} \tag{A13}$$

$$k_{chem} = k_{chem,0} exp\left[\frac{-E_{chem}}{RT_0}\left(\frac{T_0}{T} - 1\right)\right] \tag{A14}$$

$$k_{phys} = k_{phys,0} exp\left[\frac{-E_{phys}}{RT_0}\left(\frac{T_0}{T} - 1\right)\right] \tag{A15}$$

A3. Methods: Heat Transfer Coefficients

The gas-to-solid h_{gs}, wall-to-gas h_{wg}, wall-to-solid h_{ws}, and steam-wall h_t heat transfer coefficients are described in the equations below:

$$Nu = \frac{h_{wg} d_p}{k_g} = 0.009 Ar^{1/2} Pr^{1/3} \tag{A16}$$

$$Nu_p = \frac{h_{gs} d_p}{k_g} = 2.0 + 1.1 Pr^{1/3} {Re_p}^{3/5} \tag{A17}$$

$$k_{pa} = (3.58 - 2.5e) k_g \left(k_s / k_g\right)^{0.46(1-e)} \tag{A18}$$

$$h_{ws} = 2\left(k_{pa} \rho_s C_{p,s} \frac{1-e}{\pi \tau}\right)^{1/2} \tag{A19}$$

$$h_t = f_b\, h_{ws} + (1 - f_b)\, h_{wg} \tag{A20}$$

where k_g and k_s denote the gas and sorbent thermal conductivities, respectively, Ar is the Archimedes number, Pr is the Prandtl number, k_{pa} is the bed's thermal conductivity at minimum fluidization velocity, f_b is the fraction of time that the heat exchanger surface contacts the solids, and τ is the average residence time of the solids contacting the heat exchanger surface. The parameters f_b and τ are given by the following relations:

$$f_b = 0.33\left[v_{mf}^2 \left(\frac{(f_n - a_h)^2}{9.8 d_p}\right)^{0.14}\right] \tag{A21}$$

$$f_n = \frac{v_g}{v_{mf}} \tag{A22}$$

$$\tau = 0.44\left[\left(\frac{9.8 d_p}{v_{mf}^2 (f_n - a_h)^2}\right)^{0.14} \left(\frac{d_p}{d_o}\right)^{0.225}\right] \tag{A23}$$

A4. Methods: Cost Model

Table A1
Utility Prices used in the Costing Model.

Utility	Price
Steam	29.29 $/(1000 kg)
Electricity	0.06 $/kWh
Cooling Water	0.354 $/GJ

A5. Methods: Techno-Economic Optimization

Table A2
MOF price and particle lifespan for moving bed optimization cases.

	MOF Price [$/kg]	Particle Lifespan [years]
Case 1	0.5	0.5
Case 2	5	0.5
Case 3	15	0.5
Case 4	30	0.5
Case 5	0.5	2
Case 6	5	2
Case 7	15	2
Case 8	30	2

A6. Results: Reaction Set Selection

Table A3
Reaction Set Selection Results.

Model [*N*,*M*]	# of Parameters	Objective Function	AIC
[1,0]	12	3.170	−3059.65
[1,1]	15	2.773	−3132.53
[2,0]	15	3.170	−3053.65
[2,1]	**18**	**1.692**	**−3417.98**
[3,0]	18	2.547	−3176.63
[2,2]	21	1.692	−3411.98
[3,1]	21	1.692	−3411.98
[4,0]	21	2.547	−3170.63
[3,2]	24	1.692	−3405.98
[4,1]	24	1.692	−3405.98
[5,0]	24	2.547	−3164.63

A7. Results: Parameter Estimation and Validation

Table A4
Estimated chemistry model parameters for $N = 2$ and $M = 1$.

Parameter	Estimated Value	Units	Lower Bound	Upper Bound
k_{0,N_1}	67.62	–	−1000	10,000
k_{0,N_2}	214.95	–	−1000	10,000
k_{0,M_1}	23.56	–	−1000	10,000
$k_{phys,0}$	3.31E-06	Pa^{-1}	−50	100
k_{1,N_1}	160.07	K	−10000	10,000
k_{1,N_2}	69.65	K	−10000	10,000
k_{1,M_1}	92.14	K	−10000	10,000
E_{phys}	16.85	kJ/mol	5	500
n_1	2.85	–	1	15
n_2	8.19	–	1	15
m_1	1	–	1	15
N_{phys}	2.59	mol/kg	0	1000
a_H	206.16	Pa	–	–
b_H	−114.18	K	–	–
$\tau_{A,0}$	−385.03	–	–	–
$\tau_{B,0}$	−204.70	–	–	–
$\tau_{A,1}$	254.09	K	–	–
$\tau_{B,0}$	132.67	K	–	–
Objective Function	1.692			

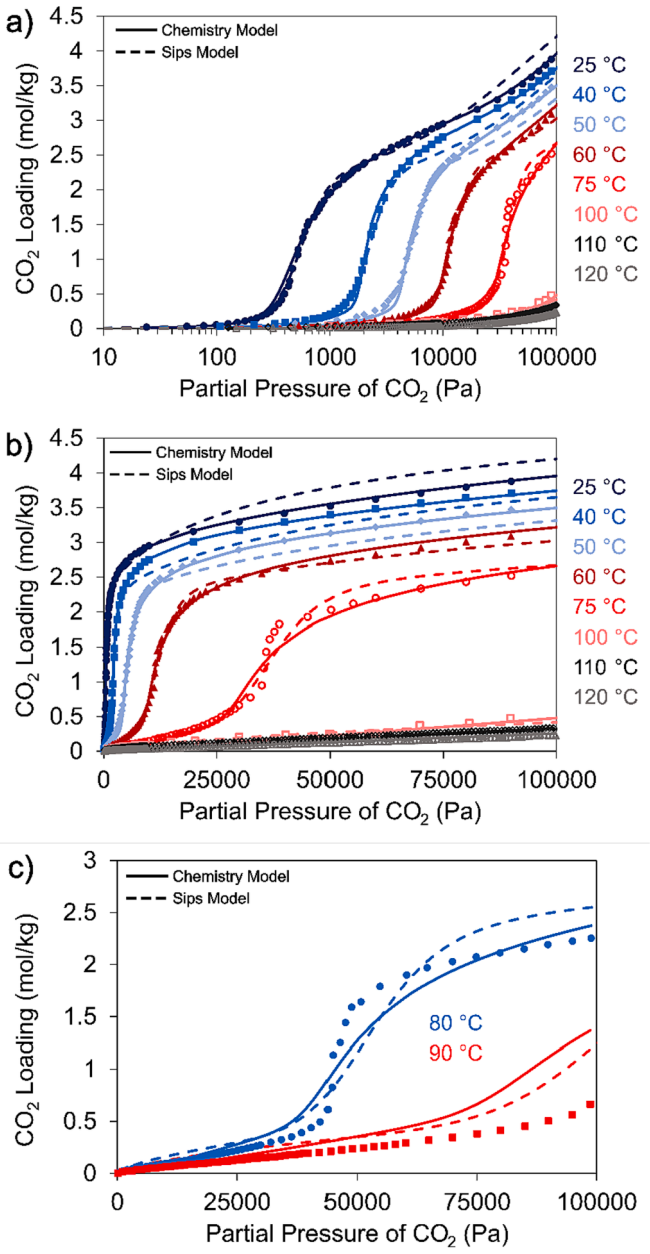

Fig. A1. Comparison of Chemistry model and Sips Isotherm model (Hughes et al., 2021). a) Estimation data with log scale horizontal axis. b) Estimation data with linear scale horizontal axis. c) Validation data. Chemistry model prediction is shown with the solid-colored lines, Sips isotherm model is shown with dashed-colored lines, and experimental data is shown with colored symbols. Temperature sets are shown with the same color.

A8. Results: Moving Bed TSA Techno-Economic Optimization

Table A5
Optimization results for each particle cost uncertainty case.

Decision Variable	Case 1	Case 2	Case 3	Case 4	Case 5	Case 6	Case 7	Case 8	Lower Bound	Upper Bound	Units
Adsorber Height	3.63	2.41	2.51	2.05	4.01	2.69	2.38	2.14	1	20	[m]
Adsorber Diameter	10.0	10.0	10.0	10.0	10.0	10.0	10.0	10.0	1	10	[m]
Adsorber Tube Pitch	0.082	0.060	0.065	0.052	0.086	0.066	0.059	0.054	0.035	0.5	[m]
Desorber Height	13.2	13.0	12.3	11.7	14.2	13.1	11.3	11.6	1	20	[m]
Desorber Diameter	10.0	10.0	10.0	10.0	10.0	10.0	10.0	10.0	1	10	[m]
Desorber Tube Pitch	0.114	0.090	0.084	0.061	0.122	0.091	0.073	0.065	0.035	0.5	[m]
Lean sorbent loading	0.388	0.485	0.513	0.553	0.369	0.433	0.540	0.518	0.025	1	[mol/kg]
Adsorber Outlet Pressure	1.01	1.01	1.01	1.01	1.01	1.01	1.01	1.01	1.01	2	[bar]
Flue Gas Flowrate	2123	1952	1984	1827	2150	2015	1935	1868	0	–	[kmol/hr]
Direct Steam Flowrate	97.6	113	110	107	97.5	109	133	106	0	–	[kmol/hr]

Table A6
Cost breakdown [$million/year] for each moving bed optimization case.

	Case 1	Case 2	Case 3	Case 4	Case 5	Case 6	Case 7	Case 8
Amortized Capital	**30.4**	**35.5**	**34.6**	**42.6**	**29.8**	**33.9**	**37.6**	**40.5**
Reactors	20.8	24.6	23.5	29.9	20.5	23.5	26.2	28.4
Blowers	0.931	0.931	0.931	0.931	0.931	0.931	0.931	0.931
Cross Exchanger	8.7	9.9	10.2	11.7	8.4	9.5	10.5	11.1
Yearly Operating Costs	**102.8**	**140.4**	**226.9**	**319.4**	**98.6**	**109.5**	**130.5**	**159.8**
Steam	93.8	95.5	96.1	97.8	93.5	94.5	96.1	96.7
Electricity	2.97	2.48	2.53	2.38	3.12	2.59	2.44	2.41
Cooling Water	0.275	0.275	0.278	0.283	0.276	0.273	0.276	0.281
Sorbent	5.79	42.2	128.0	219.0	1.70	12.1	31.7	60.4
EAOC	**133.3**	**175.8**	**261.5**	**362.0**	**128.4**	**143.5**	**168.1**	**200.3**

Table A7
EAOC [$million/year] for capital cost uncertainty cases.

	+50% Capital Costs	Nominal	−50% Capital Costs
Case 1	142.4	133.3	124.2
Case 2	186.7	175.8	164.9
Case 3	271.9	261.5	251.2
Case 4	375.4	362.0	348.5
Case 5	137.4	128.4	119.5
Case 6	153.8	143.5	133.1
Case 7	179.8	168.1	156.5
Case 8	213.0	200.3	187.5

References

Abdollahi-Govar, A., Ebner, A.D., Ritter, J.A., 2015. New Kinetic model that describes the reversible adsorption and desorption behavior of CO $_2$ in a solid amine sorbent. Energy Fuels 29, 4492–4502. https://doi.org/10.1021/acs.energyfuels.5b01119.

Akaike, H., 1974. A new look at the statistical model identification. IEEE Trans. Automat. Contr. 19, 716–723. https://doi.org/10.1109/TAC.1974.1100705.

Baskakov, A.P., Berg, B.V., Vitt, O.K., Filippovsky, N.F., Kirakosyan, V.A., Goldobin, J.M., Maskaev, V.K., 1973. Heat transfer to objects immersed in fluidized beds. Powder Technol. 8, 273–282. https://doi.org/10.1016/0032-5910(73)80092-0.

Bhattacharyya, D., Miller, D.C., 2017. Post-combustion CO_2 capture technologies — a review of processes for solvent-based and sorbent-based CO_2 capture. Current Opinion in Chemical Engineering, Energy and Environmental Engineering / Reaction Engineering and Catalysis 17, 78–92. https://doi.org/10.1016/j.coche.2017.06.005.

Chen, J.C., Grace, J.R., Golriz, M.R., 2005. Heat transfer in fluidized beds: design methods. Powder Technol. 150, 123–132. https://doi.org/10.1016/j.powtec.2004.11.035.

Denn, M.M., Yu, W.-C., Wei, J., 1979. Parameter sensitivity and kinetics-free modeling of moving bed coal gasifiers. Ind. Eng. Chem. Fund. 18, 286–288. https://doi.org/10.1021/i160071a016.

Foo, K.Y., Hameed, B.H., 2010. Insights into the modeling of adsorption isotherm systems. Chem. Eng. J. 156, 2–10. https://doi.org/10.1016/j.cej.2009.09.013.

Forse, A.C., Milner, P.J., Lee, J.-H., Redfearn, H.N., Oktawiec, J., Siegelman, R.L., Martell, J.D., Dinakar, B., Porter-Zasada, L.B., Gonzalez, M.I., Neaton, J.B., Long, J. R., Reimer, J.A., 2018. Elucidating CO2 chemisorption in diamine-appended metal-organic frameworks. J. Am. Chem. Soc. 140, 18016–18031. https://doi.org/10.1021/jacs.8b10203.

Fout, T., Zoelle, A., Keairns, D., Pinkerton, L.L., Turner, M.J., Woods, M., Kuehn, N., Shah, V., Chou, V., 2015. Cost and performance baseline for fossil energy plants volume 1a: bituminous coal (PC). And Natural Gas to Electricity Revision 3 No. DOE/NETL-2015/1723, 1480987. https://doi.org/10.2172/1480987.

Ga, S., Lee, S., Park, G., Kim, J., Realff, M., Lee, J.H., 2021. New model for S-shaped isotherm data and its application to process modeling using IAST. Chem. Eng. J. 420, 127580 https://doi.org/10.1016/j.cej.2020.127580.

Hart, W.E., Laird, C.D., Watson, J.-P., Woodruff, D.L., Hackebeil, G.A., Nicholson, B.L., Siirola, J.D., 2017. Pyomo — Optimization Modeling in Python, 2nd ed, Springer Optimization and Its Applications. Springer International Publishing. https://doi.org/10.1007/978-3-319-58821-6.

Hefti, M., Joss, L., Bjelobrk, Z., Mazzotti, M., 2016. On the potential of phase-change adsorbents for CO_2 capture by temperature swing adsorption. Faraday Discuss. 192, 153–179. https://doi.org/10.1039/C6FD00040A.

Hughes, R., Kotamreddy, G., Ostace, A., Bhattacharyya, D., Siegelman, R.L., Parker, S.T., Didas, S.A., Long, J.R., Omell, B., Matuszewski, M., 2021. Isotherm, kinetic, process modeling, and techno-economic analysis of a diamine-appended metal-organic framework for CO2 capture using fixed bed contactors. Energy Fuels 35, 6040–6055. https://doi.org/10.1021/acs.energyfuels.0c04359.

Joss, L., Hefti, M., Bjelobrk, Z., Mazzotti, M., 2017. On the potential of phase-change adsorbents for CO_2 capture by temperature swing adsorption. Energy Procedia 114, 2271–2278. https://doi.org/10.1016/j.egypro.2017.03.1375.

Kakac, S., Liu, H., Pramuanjaroenkij, A., 2012. Heat Exchangers: Selection, Rating, and Thermal Design, 3rd ed. CRC Press.

Kim, H., Miller, D.C., Modekurti, S., Omell, B., Bhattacharyya, D., Zitney, S.E., 2016. Mathematical modeling of a moving bed reactor for post-combustion CO_2 capture. AIChE J. 62, 3899–3914. https://doi.org/10.1002/aic.15289.

Kim, E.J., Siegelman, R.L., Jiang, H.Z.H., Forse, A.C., Lee, J.-H., Martell, J.D., Milner, P. J., Falkowski, J.M., Neaton, J.B., Reimer, J.A., Weston, S.C., Long, J.R., 2020. Cooperative carbon capture and steam regeneration with tetraamine-appended metal–organic frameworks. Science 392–396. https://doi.org/10.1126/science.abb3976.

Kim, K., Son, Y., Lee, W.B., Lee, K.S., 2013. Moving bed adsorption process with internal heat integration for carbon dioxide capture. Int. J. Greenhouse Gas Control 17, 13–24. https://doi.org/10.1016/j.ijggc.2013.04.005.

Knaebel, K.S., 2009. Temperature swing adsorption system. US 7,594,956 B2.

Kotamreddy, G., 2021. Process Modeling and Techno-Economic Analysis of Micro-Encapsulated Carbon Sorbents (MECS) for CO2 capture in a Fixed Bed and Moving Bed Reactors. West Virginia University.

Kotamreddy, G., Hughes, R., Bhattacharyya, D., Stolaroff, J., Hornbostel, K., Matuszewski, M., Omell, B., 2019. Process modeling and techno-economic analysis of a CO_2 capture process using fixed bed reactors with a microencapsulated solvent. Energy Fuels 33, 7534–7549. https://doi.org/10.1021/acs.energyfuels.9b01255.

Ku, Y., Wu, H.-C., Chiu, P.-C., Tseng, Y.-H., Kuo, Y.-L., 2014. Methane combustion by moving bed fuel reactor with Fe_2O_3/Al_2O_3 oxygen carriers. Appl. Energy 113, 1909–1915. https://doi.org/10.1016/j.apenergy.2013.06.014.

Kundu, J., Stilck, J.F., Lee, J.-H., Neaton, J.B., Prendergast, D., Whitelam, S., 2018. Cooperative gas adsorption without a phase transition in metal-organic frameworks. Phys. Rev. Lett. 121, 015701 https://doi.org/10.1103/PhysRevLett.121.015701.

Kunii, D., Levenspiel, O., 1991. Fluidization Engineering. Elsevier.

Lee, K.B., Beaver, M.G., Caram, H.S., Sircar, S., 2007a. Chemisorption of carbon dioxide on sodium oxide promoted alumina. AIChE J. 53, 2824–2831. https://doi.org/10.1002/aic.11312.

Lee, K.B., Beaver, M.G., 2008. Effect of reaction temperature on the performance of thermal swing sorption-enhanced reaction process for simultaneous production of fuel-cell-grade H_2 and compressed CO_2 from synthesis gas. Ind. Eng. Chem. Res. 47, 6759–6764. https://doi.org/10.1021/ie071372k.

Lee, K.B., Verdooren, A., Caram, H.S., Sircar, S., 2007b. Chemisorption of carbon dioxide on potassium-carbonate-promoted hydrotalcite. J. Colloid Interface Sci. 308, 30–39. https://doi.org/10.1016/j.jcis.2006.11.011.

Liu, S., 2015. Cooperative adsorption on solid surfaces. J. Colloid Interface Sci. 450, 224–238. https://doi.org/10.1016/j.jcis.2015.03.013.

Marshall, B.D., 2022. A Cluster based cooperative kinetic model for CO2 adsorption on amine functionalized metal-organic frameworks. Ind. Eng. Chem. Res. acs.iecr.2c02402 https://doi.org/10.1021/acs.iecr.2c02402.

McDonald, T.M., Lee, W.R., Mason, J.A., Wiers, B.M., Hong, C.S., Long, J.R., 2012. Capture of carbon dioxide from air and flue gas in the alkylamine-appended metal-

organic framework mmen-Mg2 (dobpdc). J. Am. Chem. Soc. 134, 7056–7065. https://doi.org/10.1021/ja300034j.
McDonald, T.M., Mason, J.A., Kong, X., Bloch, E.D., Gygi, D., Dani, A., Crocellà, V., Giordanino, F., Odoh, S.O., Drisdell, W.S., Vlaisavljevich, B., Dzubak, A.L., Poloni, R., Schnell, S.K., Planas, N., Lee, K., Pascal, T., Wan, L.F., Prendergast, D., Neaton, J.B., Smit, B., Kortright, J.B., Gagliardi, L., Bordiga, S., Reimer, J.A., Long, J. R., 2015. Cooperative insertion of CO_2 in diamine-appended metal-organic frameworks. Nature 519, 303–308. https://doi.org/10.1038/nature14327.
Miller, D.C., Agarwal, D., Bhattacharyya, D., Boverhof, J., Chen, Y., Eslick, J.C., Leek, J., Ma, J., Mahapatra, P., Ng, B., Sahinidis, N.V., Tong, C., Zitney, S.E., 2017. Innovative computational tools and models for the design, optimization and control of carbon capture processes.
Milner, P.J., Siegelman, R.L., Forse, A.C., Gonzalez, M.I., Runčevski, T., Martell, J.D., Reimer, J.A., Long, J.R., 2017. A diaminopropane-appended metal-organic framework enabling efficient CO2 capture from coal flue gas via a mixed adsorption mechanism. J. Am. Chem. Soc. 139, 13541–13553. https://doi.org/10.1021/jacs.7b07612.
Mondino, G., Grande, C.A., Blom, R., 2017. Effect of gas recycling on the performance of a moving bed temperature-swing (MBTSA) process for CO2 capture in a coal fired power plant context. Energies 10, 745. https://doi.org/10.3390/en10060745.
Mondino, G., Spjelkavik, A.I., Didriksen, T., Krishnamurthy, S., Stensrød, R.E., Grande, C. A., Nord, L.O., Blom, R., 2020. Production of MOF adsorbent spheres and comparison of their performance with zeolite 13X in a moving-bed TSA process for postcombustion CO_2 capture. Ind. Eng. Chem. Res. 59, 7198–7211. https://doi.org/10.1021/acs.iecr.9b06387.
Morales-Ospino, R., Santos, V.N., Lima, A.R.A., Torres, A.E.B., Vilarrasa-García, E., Bastos-Neto, M., Cavalcante, C.L., Azevedo, D.C.S., Marques, C.R.M., de Aquino, T. F., Vasconcelos, L.B., Knaebel, K.S., 2021. Parametric analysis of a moving bed temperature swing adsorption (MBTSA) process for postcombustion CO2 capture. Ind. Eng. Chem. Res. 60, 10736–10752. https://doi.org/10.1021/acs.iecr.0c05067.
Morgan, J.C., Chinen, A.S., Omell, B., Bhattacharyya, D., Tong, C., Miller, D.C., 2017. Thermodynamic modeling and uncertainty quantification of CO_2-loaded aqueous MEA solutions. Chem. Eng. Sci. 168, 309–324. https://doi.org/10.1016/j.ces.2017.04.049.
O'Connell, J.P., Haile, J.M., 2005. Thermodynamics: Fundamentals for Applications, 1st ed. Cambridge University Press. https://doi.org/10.1017/CBO9780511840234.
Okumura, T., Ogino, T., Nishibe, S., Nonaka, Y., Shoji, T., Higashi, T., 2014. CO_2 capture test for a moving-bed system utilizing low-temperature steam. Energy Procedia 63, 2249–2254. https://doi.org/10.1016/j.egypro.2014.11.243.
Ostace, A., Lee, A., Okoli, C.O., Burgard, A.P., Miller, D.C., Bhattacharyya, D., 2018. Mathematical modeling of a moving-bed reactor for chemical looping combustion of methane, in. Computer Aided Chemical Engineering. Elsevier 325–330. https://doi.org/10.1016/B978-0-444-64241-7.50049-5.
Pai, K.N., Baboolal, J.D., Sharp, D.A., Rajendran, A., 2019. Evaluation of diamine-appended metal-organic frameworks for post-combustion CO_2 capture by vacuum swing adsorption. Sep. and Pur. Tech. 211, 540–550. https://doi.org/10.1016/j.seppur.2018.10.015.
Parker, S.T., Smith, A., Forse, A.C., Liao, W.-C., Brown-Altvater, F., Siegelman, R.L., Kim, E.J., Zill, N.A., Zhang, W., Neaton, J.B., Reimer, J.A., Long, J.R., 2022. Evaluation of the stability of diamine-appended Mg 2 (dobpdc) frameworks to sulfur dioxide. J. Am. Chem. Soc. jacs.2c07498 https://doi.org/10.1021/jacs.2c07498.
Powell, M.J.D., 2009. The BOBYQA Algorithm for Bound Constrained Optimization Without Derivatives. Technical Report, Department of Applied Mathematics and Theoretical Physics. University of Cambridge.
Ruthven, D.M., 1984. Principles of Adsorption and Adsorption Processes. John Wiley & Sons.
Shirzad, M., Karimi, M., Silva, J.A.C., Rodrigues, A.E., 2019. Moving bed reactors: challenges and progress of experimental and theoretical studies in a century of research. Ind. Eng. Chem. Res. 58, 9179–9198. https://doi.org/10.1021/acs.iecr.9b01136.
Siegelman, R.L., McDonald, T.M., Gonzalez, M.I., Martell, J.D., Milner, P.J., Mason, J.A., Berger, A.H., Bhown, A.S., Long, J.R., 2017. Controlling cooperative CO2 adsorption in diamine-appended Mg2 (dobpdc) metal-organic frameworks. J. Am. Chem. Soc. 139, 10526–10538. https://doi.org/10.1021/jacs.7b05858.
Sumida, K., Rogow, D.L., Mason, J.A., McDonald, T.M., Bloch, E.D., Herm, Z.R., Bae, T.-H., Long, J.R., 2012. Carbon dioxide capture in metal-organic frameworks. Chem. Rev. 112, 724–781. https://doi.org/10.1021/cr2003272.
Turton, R., Shaeiwitz, J.A., Bhattacharyya, D., Whiting, W.B., 2018. Analysis, Synthesis, and Design of Chemical Processes, Fifth Edition. Prentice Hall.
Valentine, J., Zoelle, A., Homsy, S., Mantripragada, H., Woods, M., Roy, N., Kilstofte, A., Sturdivan, M., Steutermann, M., Fout, T., 2022. Direct Air Capture Case Studies: Sorbent System (No. DOE/NETL-2021/2865, 1879535). https://doi.org/10.2172/1879535.
Wächter, A., Biegler, L.T., 2006. On the implementation of an interior-point filter line-search algorithm for large-scale nonlinear programming. Math. Program. 106, 25–57. https://doi.org/10.1007/s10107-004-0559-y.
Weiss, J.N., 1997. The Hill equation revisited: uses and misuses. FASEB J. 11, 835–841. https://doi.org/10.1096/fasebj.11.11.9285481.
Yoon, H., Wei, J., Denn, M.M., 1978. A model for moving-bed coal gasification reactors. AIChE J. 24, 885–903. https://doi.org/10.1002/aic.690240515.
Yoon, H., Wei, J., Denn, M.M., 1979a. Transient behavior of moving-bed coal gasification reactors. AIChE J. 25, 429–439. https://doi.org/10.1002/aic.690250307.
Yoon, H., Wei, J., Denn, M.M., 1979b. Feasible operating regions for moving bed coal gasification reactors. Ind. Eng. Chem. Proc. Des. Dev. 18, 306–312. https://doi.org/10.1021/i260070a023.